Article
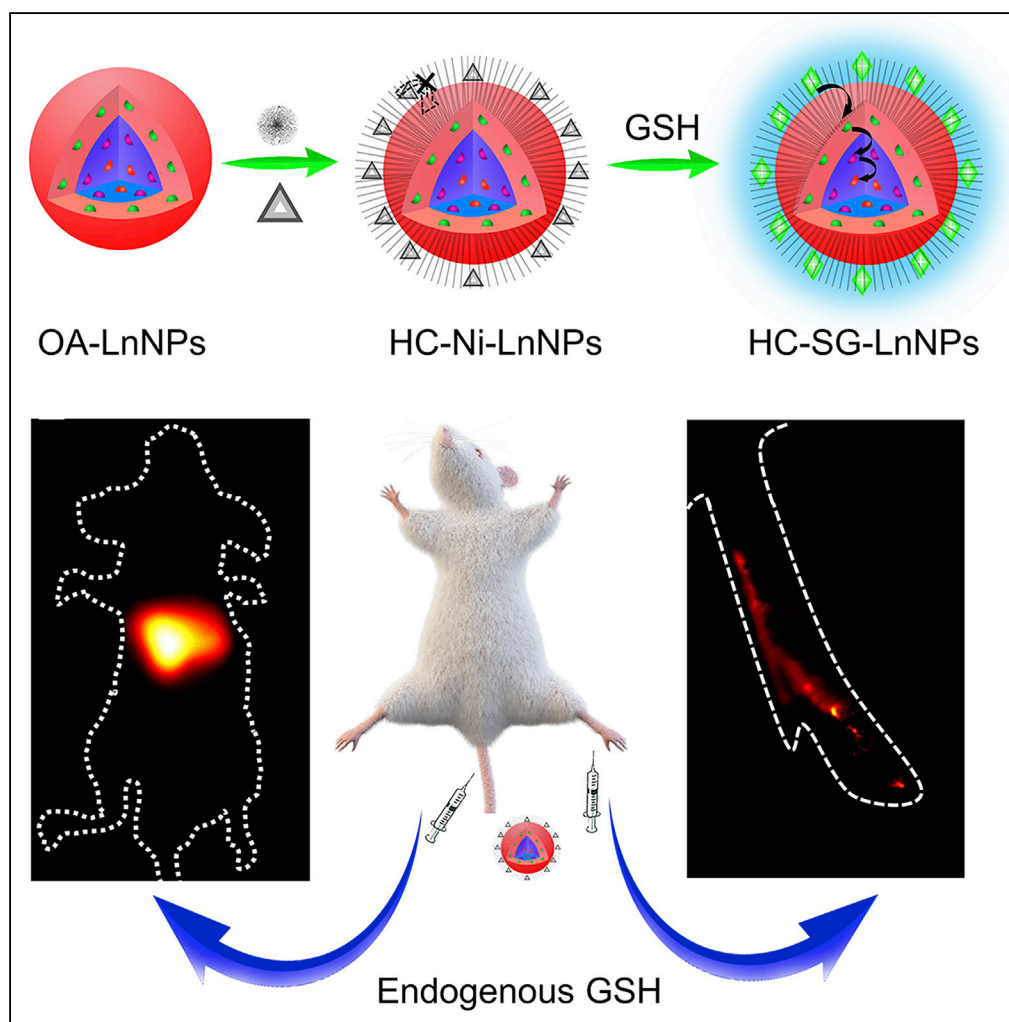
A Universal Strategy to Construct Lanthanide-Doped Nanoparticles-Based Activable NIR-II Luminescence Probe for Bioimaging

Zhen Li, Junjie Wu, Qirong Wang, Tao Liang, Juan Ge, Peipei Wang, Zhihong Liu

zhhliu@whu.edu.cn

HIGHLIGHTS

A universal strategy was proposed to construct LnNPs-based activable NIR-II probe

The strategy circumvents the difficulty in designing activable probe in NIR-II region

This probe can be applied to monitor the subtle fluctuation of GSH level *in vivo*

It shows excellent performance in bioimaging with deep penetration and high contrast

Article

A Universal Strategy to Construct Lanthanide-Doped Nanoparticles-Based Activable NIR-II Luminescence Probe for Bioimaging

Zhen Li,[1] Junjie Wu,[1] Qirong Wang,[1] Tao Liang,[2] Juan Ge,[1] Peipei Wang,[2] and Zhihong Liu[1,2,3,*]

SUMMARY

Lanthanide-doped nanoparticles (LnNPs) have gained increasing attention recently for bioimaging in the second near-infrared window (NIR-II, 1,000–1,700 nm) because of their excellent photophysical properties, but the construction of LnNPs-based activable probe responding to specific targets remains a challenge. Herein, we proposed an uncomplicated and universal strategy to fabricate LnNPs-based NIR-II probes by target-triggered dye-sensitization process. The dye acts as both the recognition motif of the target and a potential antenna for LnNPs, which can be activated by the target to sensitize the NIR-II luminescence of LnNPs. A proof-of-concept probe for glutathione (GSH) was constructed to validate this approach. It was able to track the fluctuation of GSH level in liver and lymphatic drainage and provide clear images with high contrast and resolution _in vivo_. This strategy can be generalized to construct NIR-II probes for various analytes by simply changing the recognition motif of the dye, greatly promoting the application of LnNPs.

INTRODUCTION

Fluorescence imaging with the features of real-time tracking, high temporal-spatial resolution, and non-invasiveness has been extensively studied and holds great promise for monitoring biological substances and processes _in vivo_ (He et al., 2018; Owens et al., 2016; Miao et al., 2017; Kim et al., 2018; Cheng et al., 2017). Especially, near-infrared fluorescence imaging in the second biological window (NIR-II), from 1,000 to 1700 nm, has evoked considerable attention for bioimaging because of its unparalleled spatial resolution (approximately 10 μm) and tissue penetration (centimeter level), benefiting from the negligible autofluorescence as well as the reduced photon absorption and scattering by biosamples (Tang et al., 2019; Yang et al., 2018; Sun et al., 2019a, 2019b; Alifu et al., 2018; Sheng et al., 2018; Antaris et al., 2016; Deng et al., 2019; Lei et al., 2019). Lanthanide-doped nanoparticles (LnNPs) as a new kind of promising NIR-II luminescent materials with tunable emission, sharp f-f emission peaks, high chemical stability and photostability, long luminescence lifetime, and low toxicity have received increasing interest in fields of chemical and biomedical science (Song et al., 2019b; Liu et al., 2018a; Wang et al., 2018; Ximendes et al., 2016, 2017; Zhang et al., 2019a; Fan et al., 2018; Fan and Zhang, 2019; Zhao et al., 2018). However, in most of the previous reports, LnNPs always acted as a fluorescent tag in _in vivo_ imaging, outputting "always-on" luminescence signals (He et al., 2019; Li et al., 2019; Dai et al., 2017; Zhao et al., 2019; Xue et al., 2018), which does not allow for the recognition of specific targets or events. This restriction is derived from the lack of flexible design strategies to construct activable LnNPs-based NIR-II probes, which require an on-site modulation of lanthanide emission by analytes. Because of the structural and spectral characteristics of lanthanide ions and LnNPs, it is a challenge to modulate such long-wavelength emissions via common fabricating principles for optical probes, such as photoinduced electron transfer or resonance energy transfer.

Researchers have recently made a number of efforts to deal with this problem. For example, Chen et al. designed a kind of NaCeF$_4$:Yb,Er nanocrystal with photoluminescence emission at 1,525 nm originating from the $^4I_{13/2} \rightarrow {}^4I_{15/2}$ transition of Er^{3+} because of the cross-relaxation between Er^{3+} and Ce^{3+} (Lei et al., 2018; Zhang et al., 2019b). After the oxidization of Ce^{3+} to Ce^{4+} by H$_2$O$_2$, the emission at 1,525 nm was quenched, enabling the detection of H$_2$O$_2$. But the application of this kind of probe is restricted since it can be utilized only for monitoring H$_2$O$_2$ or H$_2$O$_2$-participated processes, and the expansibility of the design is somewhat limited. Besides, Zhang et al. proposed a relatively more flexible strategy, named absorption competition-induced emission (ACIE), to build LnNPs-based NIR-II probes, in which the

[1]Ministry of Education Key Laboratory for the Synthesis and Application of Organic Functional Molecules and College of Chemistry and Chemical Engineering, Hubei University, Wuhan 430062, China
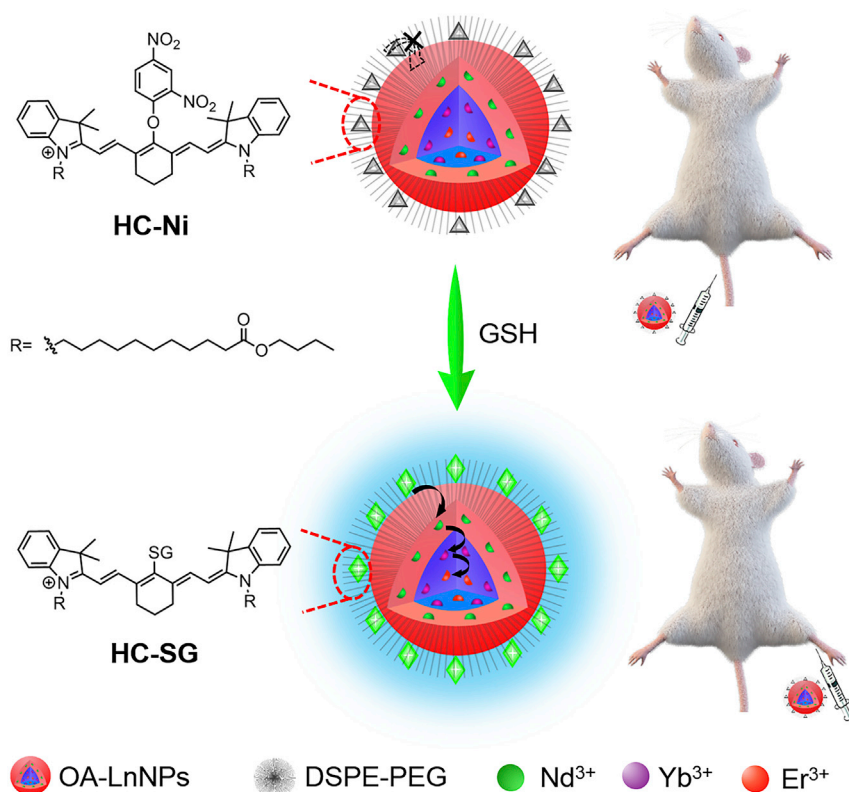
[2]Key Laboratory of Analytical Chemistry for Biology and Medicine (Ministry of Education), College of Chemistry and Molecular Sciences, Wuhan University, Wuhan 430072, China

[3]Lead Contact

*Correspondence: zhhliu@whu.edu.cn

Scheme 1. Schematic Illustration of the LnNPs-Based Activable NIR-II Luminescence Probe
The design strategy of probe is based on a target-triggered dye-sensitization process.

target was detected through regulating the filtration effect of excitation light by dyes (Wang et al., 2017, 2019). The occurrence of efficient filtration effect normally requires a high concentration of dye, which may add difficulties in the fabrication of probe for *in vivo* usage.

Herein, we propose a universal strategy for fabricating LnNPs-based activable NIR-II luminescence probe through target-regulated dye sensitization of Ln^{3+} emission. As well recognized, the faint absorptivity of lanthanide ions leads to a rather low photoluminescence efficiency of LnNPs. Through the introduction of an organic dye with strong NIR absorption as an antenna, it is possible to increase the utilizing efficiency of excitation light and enhance the luminescence of LnNPs (Zou et al., 2012; Wu et al., 2016; Liu et al., 2018b; Zhang et al., 2019c). In this sensitization process, the dyes harvest energy from external photons and subsequently transfer their excited-state energy to the ions in LnNPs (such as Nd^{3+} or Yb^{3+}) via a resonance energy transfer process (Xu et al., 2017a; Liang et al., 2018; Song et al., 2019a; Shao et al., 2016; Wei et al., 2016). A prerequisite of such sensitization is the spectral match between the emission of the dye and the absorption of Ln^{3+}. We thus consider modulating the NIR-II luminescence of LnNPs through handling the emission of a dye. In this way, the sensitization process can be readily regulated by a target specifically reacting with the dye, so as to construct an activable LnNPs-based NIR-II probe. To verify our design strategy, a proof-of-concept probe was built for detection of glutathione (GSH), which is crucial in maintaining the intracellular redox homeostasis (Lu, 2009; Estrela et al., 2006). As shown in Scheme 1, a non-emissive dye, HC-Ni, was designed as both the recognition motif for GSH and a potential antenna, which cannot sensitize the NIR-II luminescence of LnNPs in its present form. After reacting with GSH, HC-Ni transferred into the emissive form, HC-SG, triggering the sensitization of NIR-II luminescence. Hence GSH can be quantitatively detected since the enhancement of NIR-II luminescence is correlated with GSH concentration. We have demonstrated excellent biocompatibility and superior performance of the proposed probe in bioimaging *in vivo*. More significantly, this strategy provides a new approach to the construction of LnNPs-based activable NIR-II probe and can be generalized to various targets by simply changing the recognition unit of the dye.
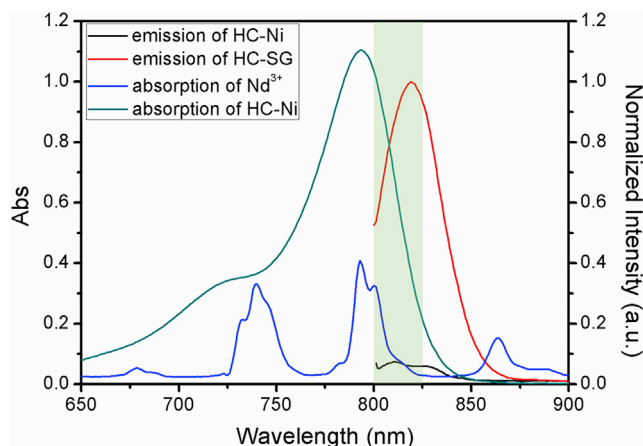
Figure 1. Spectral Properties of the Antenna

Emission of **HC-SG** overlaps well with the absorption of Nd^{3+}, but **HC-Ni** is non-emissive. And **HC-SG** shows an intense absorption band around 800 nm matching with the excitation light.

RESULTS

Photophysical Property of HC-Ni and Its Response to GSH

HC-Ni was designed as the potential antenna with a heptamethine cyanine as the fluorophore and an *m*-dinitrophenol motif as the recognition unit. Owing to the large spectral overlap between the emission spectrum of heptamethine cyanine and the absorption spectrum of Nd^{3+}, the excited-state energy of heptamethine cyanine can be effectively transferred to LnNPs through a non-radiative energy transfer process (Chen et al., 2015; Xu et al., 2017b). Introduction of the *m*-dinitrophenol into heptamethine cyanine quenches its fluorescence to generate the non-emissive **HC-Ni** due to the photoinduced electron transfer (PET) process. As shown in Figure S1A, **HC-Ni** displayed an intense absorption peak at 794 nm with a molar absorption coefficient of 2.27×10^5 $mol^{-1} \cdot L \cdot cm^{-1}$ (Figure S1B). At the wavelength of excitation light (808 nm), the molar absorption coefficient of **HC-Ni** was as high as 1.59×10^5 $mol^{-1} \cdot L \cdot cm^{-1}$ (Figure S1C), which was at least five orders of magnitude higher than that of Nd^{3+} ions (0.77 $mol^{-1} \cdot L \cdot cm^{-1}$, Figure S1D). Such a high molar absorption coefficient suggested the possibility of **HC-Ni** to act as the potential antenna. After reacting with GSH, the photoluminescence intensity of the reaction product **HC-SG** at 819 nm obviously increased in accordance with the concentration of GSH, owing to the substitution of *m*-dinitrophenol by GSH and the inhibition of PET process (Figures S2A and S2B). As shown in Figure 1, the emission peak of **HC-SG** matched well with the absorption spectrum of Nd^{3+}, fulfilling the prerequisite of non-radiative energy transfer from **HC-SG** to LnNPs. Meanwhile, the absorbance of **HC-SG** at 794 nm only changed slightly (Figures S2C and S2D). Therefore, with the intense absorption and strong emission at appropriate wavelengths, the reaction product **HC-SG** can function as an efficient antenna to sensitize the NIR-II luminescence of LnNPs. To achieve the assembly between **HC-Ni** and LnNPs, two long hydrophobic alkyl chains were introduced into **HC-Ni** to combine with LnNPs through hydrophobic interaction (vide infra).

Fabrication and Characterization of HC-Ni-LnNPs

To establish the energy-transfer chain of dye $\rightarrow Nd^{3+} \rightarrow Yb^{3+} \rightarrow Er^{3+}$ (Figure S3), we designed LnNPs with a core-shell structure of $NaYF_4$:20%Yb,2%Er@$NaYF_4$:30%Nd. The transmission electron microcopy (TEM) images illustrated the obtained LnNPs were spherical with uniform size (Figures 2A and 2B). According to the size histograms, the diameter of LnNPs was 36.8 nm with a core of 33.6 nm and a shell thickness of 1.6 nm (Figures 2C and 2D). The crystal phase of core and core-shell structured LnNPs was characterized by X-ray diffraction (XRD) patterns (Figure 2E), which were both consistent with the hexagonal-phase of $NaYF_4$ (JCPDS No. 16-0334). Then, **HC-Ni** and oleic acid (OA)-coated LnNPs were assembled through hydrophobic interaction and coated with an amphiphilic molecule DSPE-PEG to obtain the water-soluble nanoprobe HC-Ni-LnNPs. TEM image and XRD analysis indicated that the modification by **HC-Ni** did not induce significant changes in shape, size, and crystallinity of LnNPs (Figures S4A and S4B). The successful construction of HC-Ni-LnNPs was confirmed by Fourier transform infrared (FTIR) spectra and UV-vis spectra. As shown in Figure 2F, the typical peak at 1,630 cm^{-1} in the FTIR spectra of HC-Ni-LnNPs were assigned to C=O of the
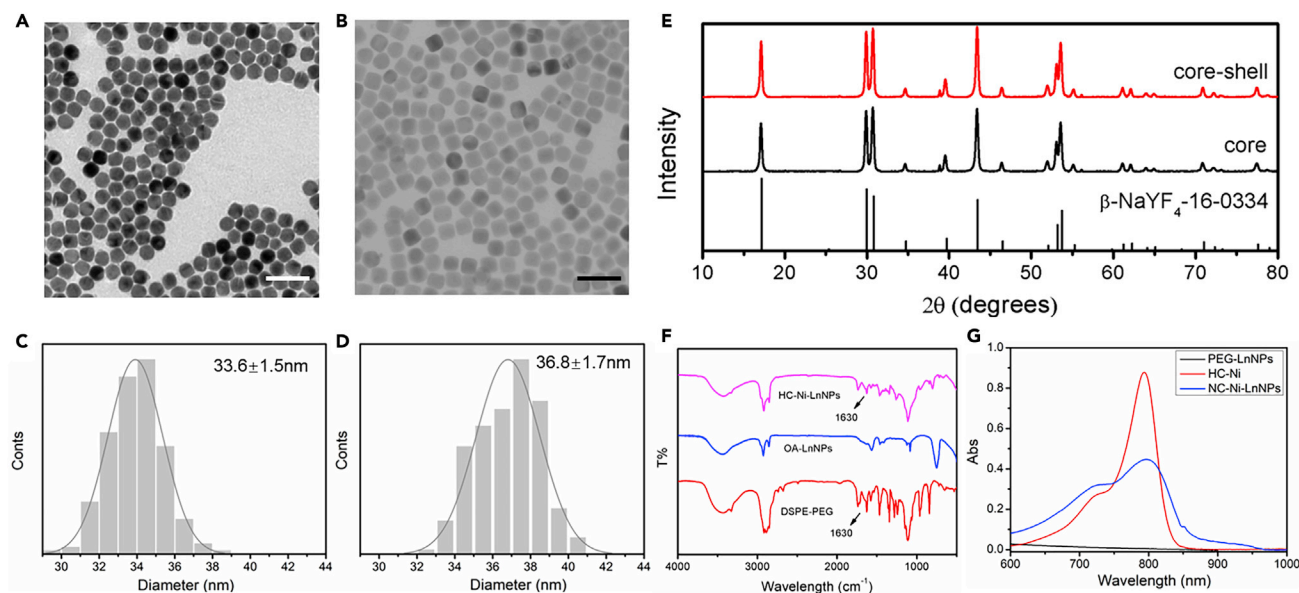
Figure 2. Characterization of LnNPs and HC-Ni-LnNPs
(A–D) TEM images and size distribution of core (A and C) and core-shell (B and D) structured LnNPs. Scale bar: 100 nm.
(E) XRD patterns of core and core-shell structured LnNPs.
(F) FTIR spectra of DSPE-PEG, OA-LnNPs, and HC-Ni-LnNPs.
(G) The UV-vis spectra of the LnNPs before and after loading with **HC-Ni**.

amide group stretching vibrations in DSPE-PEG, confirming its existence on the surface of HC-Ni-LnNPs. Meanwhile, the absorption around 800 nm of **HC-Ni** appeared on the spectrum of HC-Ni-LnNPs (Figure 2G). In addition, because of the positive charge of **HC-Ni**, the ζ potential of DSPE-PEG-coated LnNPs shifted from -1.8 mV to $+30$ mV after **HC-Ni** loading (Figure S5). All the above results confirmed that the HC-Ni-LnNPs nanoprobe was successfully constructed.

Sensing of GSH in Solution

Then, we investigated the sensing ability of HC-Ni-LnNPs for GSH in buffer solution. First, we optimized the structure of LnNPs including the amount of Nd^{3+} in shell and the thickness of shell, which decided the sensitization efficiency. In the energy transfer process, Nd^{3+} ions absorb the excited-state energy of dyes and subsequently transfer their energy to Yb^{3+} ions. Thus, a high concentration of Nd^{3+} will favor this process owing to the enhanced ability of energy harvesting and rate of energy transfer from Nd^{3+} to Yb^{3+}. However, the detrimental cross-relaxation process between Nd^{3+} ions ($^4F_{3/2}+^4I_{9/2} \rightarrow 2^4I_{15/2}$) may arise with elevating the Nd^{3+} concentration, which will invalidate the energy harvested by Nd^{3+} (Chen et al., 2015). Therefore, for purpose of optimization, we prepared a series of core-shell structured LnNPs, $NaYF_4$:20%Yb,2%Er@-$NaYF_4$:x%Nd (x = 10, 20, 30, 40, 50 and 60, respectively), with core diameter of 33.9 nm and shell thickness of about 2 nm (Figure S6). As shown in Figure 3A, at the Nd^{3+} concentration of 30%, a balance between the two effects can be obtained, achieving the maximal luminescence enhancement factor (F/F$_0$, in which F and F$_0$ are the luminescence intensity at 1,530 nm with and without GSH, respectively, termed as LEF below). The corresponding NIR-II luminescence spectra are shown in Figure S7. Furthermore, the shell thickness of LnNPs can significantly affect the performance of the probe. As known, since the non-radiative energy transfer process is highly dependent on the distance of energy donor-acceptor pair, a thinner shell is beneficial for the effective energy transfer from dye to Nd^{3+} and Nd^{3+} to Yb^{3+}. However, a thinner shell layer will cause more serious surface quenching of luminescence. With the fixed size of the core, we synthesized four groups of core-shell structured LnNPs with the shell thickness of 1.9, 3.1, 3.9, and 5.6 nm, respectively (Figure S8). As shown in Figure 3B, the best response performance was achieved with the shell thickness of 3.1 nm (the corresponding NIR-II luminescence spectra are shown in Figure S9).

With the optimal structure of LnNPs, we investigated the influence of the loading capacity of **HC-Ni** assembled on the surface of LnNPs on the response performance. According to the molar absorption coefficient of **HC-Ni** and the absorbance of HC-Ni-LnNPs at 794 nm, the loading capacities of **HC-Ni** for the five
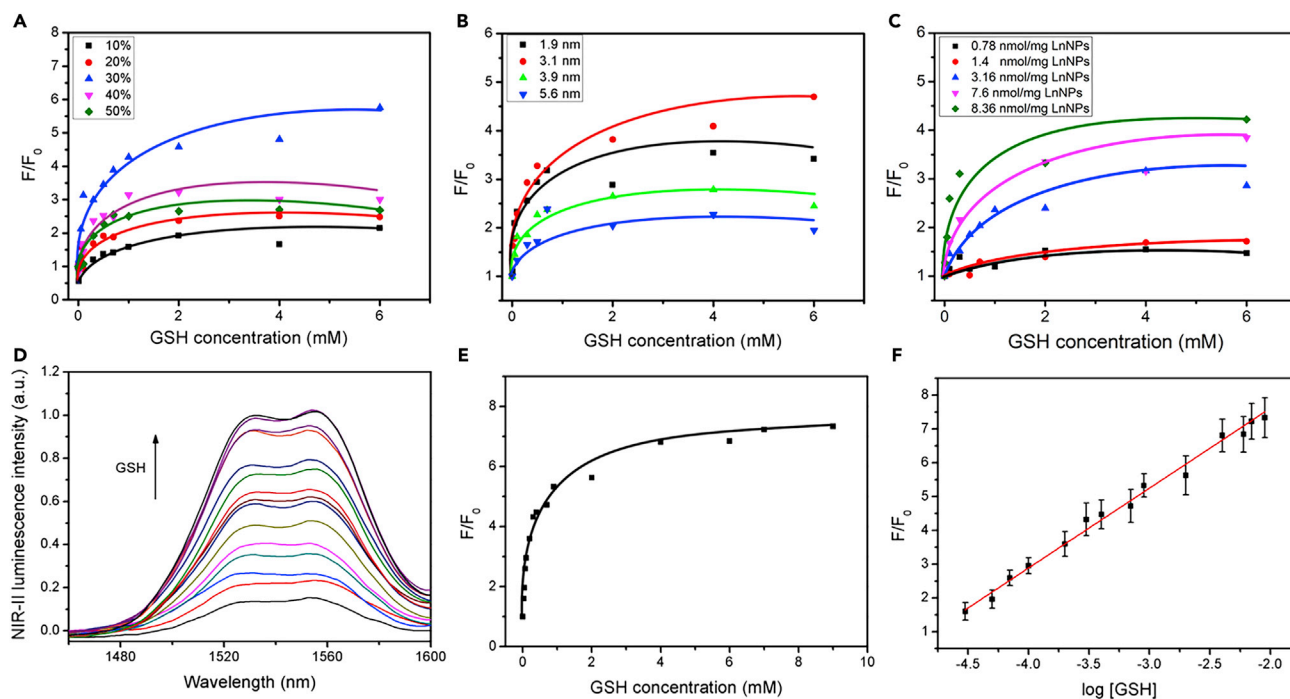
Figure 3. Sensing of GSH in Solution

(A–C) Luminescence enhancement factor (LEF), F/F_0, at 1,530 nm of HC-Ni-LnNPs responding to GSH with (A) different Nd^{3+} doping concentrations of LnNPs; (B) various shell thickness of LnNPs; (C) different loading capacity of **HC-Ni**.

(D) NIR-II luminescence spectra of HC-Ni-LnNPs responding to GSH under the optimal conditions.

(E and F) (E) Dependence of F/F_0 at 1,530 nm of HC-Ni-LnNPs on the GSH concentration and (F) the linear relationship between F/F_0 and logarithm of GSH concentration. Data are represented as mean ± SD (n = 3).

batches of probes prepared were calculated as 0.78, 1.4, 3.16, 7.6, and 8.36 nmol/mg LnNPs, respectively (Figure S10). As shown in Figure 3C, the LEF increased with enhancing the amount of **HC-Ni** loaded on the surface of nanoprobe. Notably, the LEF reached the maximum at a loading capacity of 8.36 nmol/mg, which was the maximal amount of **HC-Ni** that could be loaded (the corresponding NIR-II luminescence spectra are shown in Figure S11). In addition, the luminescence of HC-Ni-LnNPs after reacting with GSH as a function of time was detected, which showed that the LEF gradually increased and reached the plateau after 50 min (Figure S12). With the above optimized experimental conditions, we recorded the NIR-II luminescence signal of HC-Ni-LnNPs after introducing various concentrations of GSH. As shown in Figure 3D, the NIR-II luminescence was enhanced stepwise with increasing the concentration of GSH. More importantly, the LEF at 1,530 nm was dependent on the concentration of GSH in the range of 0.03–9 mM (Figure 3E), implying the feasibility of quantitatively detecting GSH. As shown in Figure 3F, the LEF exhibited a good linear relationship with the logarithm of [GSH] and the detection limit was calculated to be 1.9 μM according to three times the standard deviation of blank signal (n = 7). In contrast, no significant luminescence response was measured after introduction of other species, such as metal ions, amino acid, reactive oxygen species (ROS), and other biothiols, suggesting the excellent specificity of HC-Ni-LnNPs (Figure S13). The energy transfer efficiency from **HC-SG** to Nd^{3+} was studied by comparing the lifetime of **HC-SG** assembled on the surface of nanoparticles with or without doping Nd^{3+}. As shown in Figure S14, the lifetime of **HC-SG** shortened from 0.92 to 0.73 ns after doping Nd^{3+}, by which an energy transfer efficiency of 20% was calculated.

Biosafety of the HC-Ni-LnNPs Probe

Before being used in bioimaging of GSH *in vivo*, the stability and biocompatibility of HC-Ni-LnNPs were first assessed. As exhibited in Figure S15, HC-Ni-LnNPs emitted stable NIR-II luminescence signals in HEPES buffer, DMEM medium, and fetal bovine serum (FBS) during 2 h incubation at 37°C. This luminescence signal also changed very slightly under different pH value from 5.7 to 8.2 (Figure S16). Furthermore, incubation of the product, HC-SG-LnNPs, at 37°C for 2 h in the above-mentioned three kinds of media did

not cause obvious variation in the luminescence signal either (Figure S17). These results demonstrated that both the probe and the reaction product possessed adequate stability and were suitable for long-term observation in bioimaging. Subsequently, the cytotoxicity of HC-Ni-LnNPs was evaluated by the cell counting kit-8 (CCK-8) assay. As shown in Figure S18, the cell viability maintained >90% after incubation with various concentrations of HC-Ni-LnNPs in the range of 0–0.6 mg/mL, illustrating the very low cytotoxicity of HC-Ni-LnNPs. This result was also in agreement with the co-staining by calcein-AM, which could stain living cells with a green fluorescence, and propidium iodide (PI), which could stain dead cells with a red fluorescence. As shown in Figure S19, strong green fluorescence and slight red fluorescence were observed with each concentration of HC-Ni-LnNPs-treated cells. Furthermore, different amounts of HC-Ni-LnNPs (0, 3, and 4.5 mg/100 g body weight) were intravenously (i.v.) injected into the tail of healthy mice to investigate the *in vivo* biosafety of this nanoprobe. After 7 days, the blood routine and blood biochemical parameters of the mice injected with HC-Ni-LnNPs or physiological saline showed no significant difference (Figure S20). The hematoxylin and eosin (H&E) staining results of the major organs including heart, liver, spleen, lung, and kidney further confirmed that HC-Ni-LnNPs did not induce obvious damage to these organs (Figure S21). All the above results revealed the excellent biocompatibility of HC-Ni-LnNPs, paving the way to apply for *in vivo* bioimaging.

In Vivo Imaging of GSH Level in Mice

With the superior response performance and biocompatibility of HC-Ni-LnNPs verified, we then examined the bioimaging capability of this NIR-II luminescence probe. First, we investigated the wavelength dependence of imaging by a tissue phantom study covered with different thicknesses of lard, which was detected by an InGaAs camera equipped with different long-pass (LP) filters (1,000, 1,100, 1,200, and 1,300 nm). Owing to the reduced scattering coefficient of NIR-II luminescence, the cuvette profiles were discernible in all images with the depth range from 0 to 4.5 mm (Figure S22A). Furthermore, the signal-to-background ratio (SBR) improved with increasing the wavelength because of the inverse wavelength dependence of scattering coefficient (Figure S22B). Therefore, the 1,300-nm LP filter was utilized in subsequent bioimaging experiments. Next, we applied this nanoprobe to track the intrinsic GSH level in the body. After i.v. injection of HC-Ni-LnNPs, the NIR-II luminescence signals of mice were recorded at different time points. As shown in Figure S23, a clear blood-vessel profile can be observed 1 min post injection (p.i.). This NIR-II luminescence signal gradually strengthened, reached a maximum at 7 min of p.i., and then decreased stepwise. Because of the lower GSH concentration in blood than in liver, the intensity of NIR-II luminescence signal in blood vessel was much weaker than that in the liver. After 20 min of p.i., the NIR-II luminescence signal was detectable mainly in the liver. We further investigated the metabolic time of HC-Ni-LnNPs in the liver. As shown in Figure S24, the NIR-II luminescence signal reached a maximum at about 3–6 h and then gradually decreased until 32 h. Taken together, the above results have shown the promising capacity of HC-Ni-LnNPs to image GSH *in vivo*.

Thereafter, we estimated the performance of the nanoprobe to sense GSH variations *in vivo*. As an initial trial, N-methylmaleimide (NMM), a thiol-blocking reagent, was utilized to modulate the GSH level in mice liver. As shown in Figure S25, the control group of mice i.v. injected with HC-Ni-LnNPs only exhibited the brightest NIR-II luminescence. The luminescence intensities of the liver region in other four groups, which were pretreated with NMM (0.5, 1, 1.5, and 2 mg/100 g body weight) for 30 min before injection of HC-Ni-LnNPs, were obviously lower than that of the control group, and the intensity decreased corresponding to the concentration of NMM administrated. Furthermore, we investigated the ability of HC-Ni-LnNPs to monitor the subtle fluctuation of GSH level in two physiological processes. In one mice model, lipopolysaccharide (LPS) was intraperitoneally (i.p.) injected into mice to induce acute inflammation, decreasing the ratio of GSH/GSSG in liver because of the activation of macrophages and neutrophils to produce ROS (Kundu et al., 2009; Yamada et al., 2006). Before i.v. injection of HC-Ni-LnNPs, the mice were pretreated with different dosages of LPS from 0 to 0.75 mg/100 g body weight for 24 h. With increasing dosage of LPS, the NIR-II luminescence signal in liver weakened gradually (Figure S26) because of the reduction of GSH content. We also recorded the luminescence signals of these four batches of samples at different time points after injecting the nanoprobe. We found that the change tendency of luminescence intensity versus the dosage of LPS was consistent at each time point (Figures S26 and S27), indicating the applicability of HC-Ni-LnNPs for long-term bioimaging *in vivo*. Another mice model was the drug overdose-induced liver injury. Acetaminophen (APAP), a painkiller that may lead to grievous damage to liver and consumption of GSH with excessive amount (Saito et al., 2010; Mitchell et al., 1985; Yin et al., 2014), was i.v. injected into the mice body to cause hepatotoxicity. As shown in Figure 4A, the normal
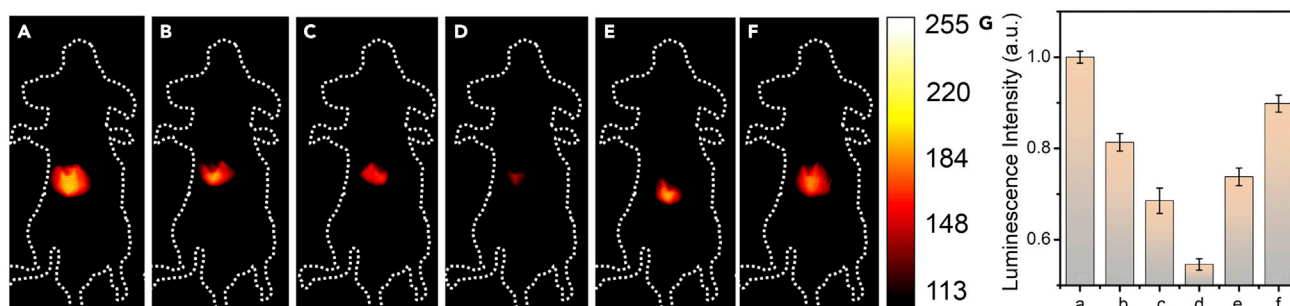
Figure 4. *In Vivo* NIR-II Luminescence Imaging of GSH in Liver Injury Model

(A–D) *In vivo* NIR-II luminescence imaging of mice injected with APAP (A: 0, B: 10, C: 20, D: 30 mg/100 g body weight) 0.5 h before loading with HC-Ni-LnNPs. (E and F) Mice injected with α-LA (E: 1; f: 2 mg/100 g body weight) 1 h before the treatment with APAP (30 mg/100 g body weight). (G) Luminescence intensities of images (A)–(F). Data are represented as mean ± SD (n = 3).

mice injected with HC-Ni-LnNPs exhibited strong NIR-II luminescence because of the high concentration of GSH in normal liver cells. For the three groups with hepatotoxicity, mice were i.v. injected with APAP at 10, 20, and 30 mg/100 g body weight, respectively, 0.5 h before loading with HC-Ni-LnNPs. As expected, the NIR-II luminescence signals of these samples gradually decreased with the increased degree of hepatotoxicity (Figures 4B–4D and 4G). As revealed in previous studies, α-lipoic acid (α-LA) was able to suppress the APAP-induced hepatotoxicity, recovering GSH level in liver cells (Abdel-Zaher et al., 2008; Xiao et al., 2015; Liang et al., 2016). Therefore, other two batches of mice were pretreated with α-LA for 1 h before injecting APAP to investigate the protective effect of α-LA with regulation of GSH level in the liver. As shown in Figures 4E and 4F, the NIR-II luminescence signals were brighter than that of the group injected with APAP at the same amount, and the intensity was enhanced corresponding to the increase of α-LA dosage. To rule out the possible effect of APAP or LPS on the NIR-II luminescence intensity of LnNPs, four sets of control experiment were conducted, where LnNPs or HC-Ni-LnNPs were incubated with APAP or LPS. As shown in Figure S28, the NIR-II luminescence of both LnNPs and HC-Ni-LnNPs kept almost unchanged. In addition, to preclude the potential contribution of ROS caused by liver failure to the luminescence change of HC-Ni-LnNPs, another control experiment was performed. The NIR-II luminescence intensity of HC-SG-LnNPs incubated with ROS was detected, which exhibited no significant change (Figure S29). All the above results have illustrated the satisfying ability of HC-Ni-LnNPs to track the fluctuation of GSH in specific processes.
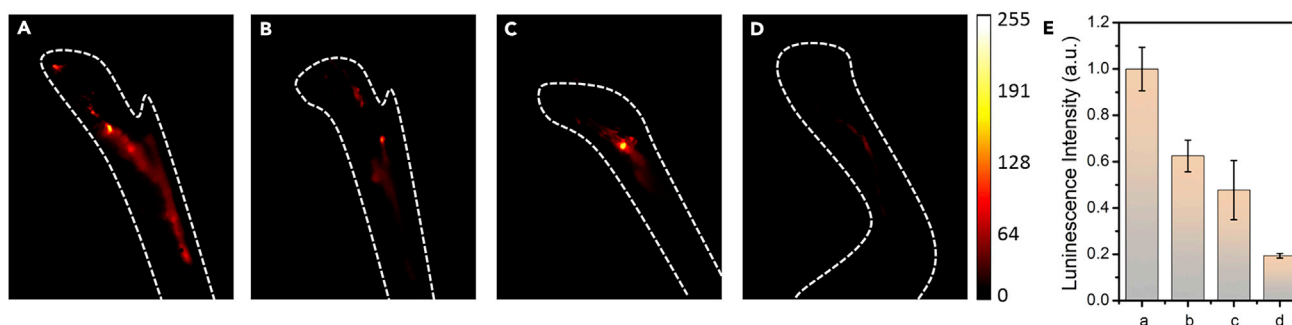
In Vivo Imaging of GSH in Lymphatic Drainage

The reduced scattering coefficient and near-zero autofluorescence endow NIR-II luminescence imaging with high spatial resolution. To demonstrate the capability of HC-Ni-LnNPs for high-resolution imaging *in vivo*, it was then applied to detect the GSH level in lymphatic drainage in the hindlimb of mice, which is composed of two connective lymph vessels and two lymph nodes and appropriate for estimating imaging resolution. The mice were intradermally (i.d.) injected with LPS (0, 0.125, 0.25, and 0.5 mg/100 g body weight) to cause lymphatic inflammation and reduce GSH level, followed by i.d. injection of HC-Ni-LnNPs 6 h later. As shown in Figure 5, the lymph structure can be observed clearly. The NIR-II luminescence intensity was the highest in the normal group and obviously weakened in the lymphatic inflammation groups. In addition, the luminescence intensities decreased in accordance with the dosage of LPS injected, revealing the different levels of LPS-induced lymphatic inflammation. These results supported the fact that the LnNPs-based NIR-II luminescence probe possessed high-resolution in bioimaging.

DISCUSSION

In summary, we proposed an uncomplicated and straightforward strategy to construct LnNPs-based activable NIR-II luminescence probe based on a target-triggered dye-sensitization process. Through regulating the emission of the dye by a specific analyte, the NIR-II luminescence of LnNPs can be readily modulated in response to the analyte. A proof-of-concept probe for GSH, namely, HC-Ni-LnNPs, was fabricated, which showed good biocompatibility and excellent response performance toward the target both *in vitro* and *in vivo*. HC-Ni-LnNPs were successfully applied in tracking the fluctuation of GSH level in the liver induced by drugs and imaging GSH with high resolution in lymphatic drainage. Our approach can be extended to construct probes for various targets by simply altering the recognition unit of the dye. We thus expect that

Figure 5. *In Vivo* NIR-II Imaging of Lymphatic Drainage in Lymphatic Inflammation Model

(A–D) Mice were i.d. injected with LPS (A: 0, b: 0.125, C: 0.25, D: 0.5 mg/100 g body weight) for 6 h before the injection of HC-Ni-LnNPs.

(E) Luminescence intensities of images (A)–(D). Data are represented as mean $\pm$ SD (n = 3).

this strategy will facilitate the design of LnNPs-based activable NIR-II luminescence probes and promote their applications in the future.

Limitations of the Study

We have proposed a universal strategy to construct LnNPs-based activable NIR-II luminescence probe through a target-triggered dye-sensitization process, by which a probe for GSH detection was fabricated. Probes for other targets have not been confirmed and are worth investigating in the future.

METHODS

All methods can be found in the accompanying Transparent Methods supplemental file.

SUPPLEMENTAL INFORMATION

Supplemental Information can be found online at https://doi.org/10.1016/j.isci.2020.100962.

AUTHOR CONTRIBUTIONS

The manuscript was written through the contributions of all the authors. All authors have given approval to the final version of the manuscript. Z. Li, J.W., Q.W., T.L., J.G., and P.W. performed the experiments. Z. Li and Z. Liu analyzed the data, wrote the manuscript, and designed the experimental approach.

DECLARATION OF INTERESTS

The authors declare no competing interest.

REFERENCES

Abdel-Zaher, A.O., Abdel-Hady, R.H., Mahmoud, M.M., and Farrag, M.M.Y. (2008). The potential protective role of alpha-lipoic acid against acetaminophen-induced hepatic and renal damage. Toxicology *243*, 261–270.

Alifu, N., Zebibula, A., Qi, J., Zhang, H., Sun, C., Yu, X., Xue, D., Lam, J.W.Y., Li, G., Qian, J., et al. (2018). Single-molecular near-infrared-II

theranostic systems: ultrastable aggregation-induced emission nanoparticles for long-term tracing and efficient photothermal therapy. ACS Nano *12*, 11282–11293.

Antaris, A.L., Chen, H., Cheng, K., Sun, Y., Hong, G., Qu, C., Diao, S., Deng, Z., Hu, X., Zhang, B., et al. (2016). A small molecule dye for NIR-II imaging. Nat. Mater. *15*, 235–242.

Chen, G., Damasco, J., Qiu, H., Shao, W., Ohulchanskyy, T.Y., Valiev, R.R., Wu, X., Han, G., Wang, Y., Yang, C., et al. (2015). Energy-cascaded upconversion in an organic dye-sensitized core/shell fluoride nanocrystal. Nano Lett. *15*, 7400–7407.

Cheng, D., Pan, Y., Wang, L., Zeng, Z., Yuan, L., Zhang, X., and Chang, Y.-T. (2017). Selective

visualization of the endogenous peroxynitrite in an inflamed mouse model by a mitochondria-targetable two-photon ratiometric fluorescent probe. J. Am. Chem. Soc. 139, 285–292.

Dai, Y., Yang, D., Yu, D., Cao, C., Wang, Q., Xie, S., Shen, L., Feng, W., and Li, F. (2017). Mussel-inspired polydopamine-coated lanthanide nanoparticles for NIR-II/CT dual imaging and photothermal therapy. ACS Appl. Mater. Interfaces 9, 26674–26683.

Deng, Z., Jiang, M., Li, Y., Liu, H., Zeng, S., and Hao, J. (2019). Endogenous H_2S-triggered in situ synthesis of NIR-II-emitting nanoprobe for in vivo intelligently lighting up colorectal cancer. iScience 17, 217–224.

Estrela, J.M., Ortega, A., and Obrador, E. (2006). Glutathione in cancer biology and therapy. Crit. Rev. Clin. Lab. Sci. 43, 143–181.

Fan, Y., Wang, P., Lu, Y., Wang, R., Zhou, L., Zheng, X., Li, X., Piper, J.A., and Zhang, F. (2018). Lifetime-engineered NIR-II nanoparticles unlock multiplexed in vivo imaging. Nat. Nanotechnol. 13, 941–946.

Fan, Y., and Zhang, F. (2019). A new generation of NIR-II probes: lanthanide-based nanocrystals for bioimaging and biosensing. Adv. Opt. Mater. 7, 1801417.

He, S., Song, J., Qu, J., and Cheng, Z. (2018). Crucial breakthrough of second near-infrared biological window fluorophores: design and synthesis toward multimodal imaging and theranostics. Chem. Soc. Rev. 47, 4258–4278.

He, S., Chen, S., Li, D., Wu, Y., Zhang, X., Liu, J., Song, J., Liu, L., Qu, J., and Cheng, Z. (2019). High affinity to skeleton rare earth doped nanoparticles for near-infrared II imaging. Nano Lett. 19, 2985–2992.

Kim, D., Kim, J., Park, Y.I., Lee, N., and Hyeon, T. (2018). Recent development of inorganic nanoparticles for biomedical imaging. ACS Cent. Sci. 4, 324–336.

Kundu, K., Knight, S.F., Willett, N., Lee, S., Taylor, W.R., and Murthy, N. (2009). Hydrocyanines: a class of fluorescent sensors that can image reactive oxygen species in cell culture, tissue, and in vivo. Angew. Chem. Int. Ed. 48, 299–303.

Lei, X., Li, R., Tu, D., Shang, X., Liu, Y., You, W., Sun, C., Zhang, F., and Chen, X. (2018). Intense near-infrared-II luminescence from $NaCeF_4$:Er/Yb nanoprobes for in vitro bioassay and in vivo bioimaging. Chem. Sci. 9, 4682–4688.

Li, Y., Zeng, S., and Hao, J. (2019). Non-invasive optical guided tumor metastasis/vessel imaging by using lanthanide nanoprobe with enhanced down-shifting emission beyond 1500 nm. ACS Nano 13, 248–259.

Liang, T., Li, Z., Song, D., Shen, L., Zhuang, Q., and Liu, Z. (2016). Modulating the luminescence of upconversion nanoparticles with heavy metal ions: a new strategy for probe design. Anal. Chem. 88, 9989–9995.

Liang, T., Li, Z., Wang, P., Zhao, F., Liu, J., and Liu, Z. (2018). Breaking through the signal-to-background limit of upconversion nanoprobes using a target-modulated sensitizing switch. J. Am. Chem. Soc. 140, 14696–14703.

Lei, Z., Sun, C., Pei, P., Wang, S., Li, D., Zhang, X., and Zhang, F. (2019). Stable, wavelength-tunable fluorescent dyes in the NIR-II region for in vivo high-contrast bioimaging and multiplexed biosensing. Angew. Chem. Int. Ed. 58, 8166–8171.

Liu, L., Wang, S., Zhao, B., Pei, P., Fan, Y., Li, X., and Zhang, F. (2018a). Er^{3+} Sensitized 1530 nm to 1180 nm second near-infrared window upconversion nanocrystals for in vivo biosensing. Angew. Chem. Int. Ed. 57, 7518–7522.

Liu, Q., Zou, X., Shi, Y., Shen, B., Cao, C., Cheng, S., Feng, W., and Li, F. (2018b). An efficient dye-sensitized NIR emissive lanthanide nanomaterial and its application in fluorescence-guided peritumoral lymph node dissection. Nanoscale 10, 12573–12581.

Lu, S.C. (2009). Regulation of glutathione synthesis. Mol. Aspects Med. 30, 42–59.

Miao, Q., Xie, C., Zhen, X., Lyu, Y., Duan, H., Liu, X., Jokerst, J.V., and Pu, K. (2017). Molecular afterglow imaging with bright, biodegradable polymer nanoparticles. Nat. Biotechnol. 35, 1102–1110.

Mitchell, D.B., Acosta, D., and Bruckner, J.V. (1985). Role of glutathione depletion in the cytotoxicity of acetaminophen in a primary culture system of rat hepatocytes. Toxicology 37, 127–146.

Owens, E.A., Henary, M., El Fakhri, G., and Choi, H.S. (2016). Tissue-specific near-infrared fluorescence imaging. Acc. Chem. Res. 49, 1731–1740.

Saito, C., Zwingmann, C., and Jaeschke, H. (2010). Novel mechanisms of protection against acetaminophen hepatotoxicity in mice by glutathione and N-acetylcysteine. Hepatology 51, 246–254.

Shao, W., Chen, G., Kuzmin, A., Kutscher, H.L., Pliss, A., Ohulchanskyy, T.Y., and anf Prasad, P.N. (2016). Tunable narrow band emissions from dye-sensitized core/shell/shell nanocrystals in the second near-infrared biological window. J. Am. Chem. Soc. 138, 16192–16195.

Sheng, Z., Guo, B., Hu, D., Xu, S., Wu, W., Liew, W.H., Yao, K., Jiang, J., Liu, C., Zheng, H., et al. (2018). Bright aggregation-induced-emission dots for targeted synergic NIR-II fluorescence and NIR-I photoacoustic imaging of orthotopic brain tumors. Adv. Mater. 30, 1800766.

Song, D., Chi, S., Li, X., Wang, C., Li, Z., and Liu, Z. (2019a). Upconversion system with quantum dots as sensitizer: improved photoluminescence and PDT efficiency. ACS Appl. Mater. Interfaces 11, 41100–41108.

Song, X., Li, S., Guo, H., You, W., Shang, X., Li, R., Tu, D., Zheng, W., Chen, Z., Yang, H., et al. (2019b). Graphene-oxide-modified lanthanide nanoprobes for tumor-targeted visible/NIR-II luminescence imaging. Angew. Chem. Int. Ed. 58, 18981–18986.

Sun, C., Li, B., Zhao, M., Wang, S., Lei, Z., Lu, L., Zhang, H., Feng, L., Dou, C., Yin, D., et al. (2019a). J-aggregates of cyanine dye for NIR-II in-vivo dynamic vascular imaging beyond 1500 nm. J. Am. Chem. Soc. 141, https://doi.org/10.1021/jacs.9b10043.

Sun, Y., Ding, F., Zhou, Z., Li, C., Pu, M., Xu, Y., Zhan, Y., Lu, X., Li, H., Yang, G., et al. (2019b). Rhomboidal Pt(II) metallacycle-based NIR-II theranostic nanoprobe for tumor diagnosis and image-guided therapy. Proc. Natl. Acad. Sci. U S A 116, 1968–1973.

Tang, Y., Pei, F., Lu, X., Fan, Q., and Huang, W. (2019). Recent advances on activatable NIR-II fluorescence probes for biomedical imaging. Adv. Opt. Mater. 7, 1900917.

Wang, P., Fan, Y., Lu, L., Liu, L., Fan, L., Zhao, M., Xie, Y., Xu, C., and Zhang, F. (2018). NIR-II nanoprobes in-vivo assembly to improve image-guided surgery for metastatic ovarian cancer. Nat. Commun. 9, 2898.

Wang, R., Zhou, L., Wang, W., Li, X., and Zhang, F. (2017). In vivo gastrointestinal drug-release monitoring through second near-infrared window fluorescent bioimaging with orally delivered microcarriers. Nat. Commun. 8, 14702.

Wang, S., Liu, L., Fan, Y., El-Toni, A.M., Alhoshan, M.S., Li, D., and Zhang, F. (2019). In vivo high-resolution ratiometric fluorescence imaging of inflammation using NIR-II nanoprobes with 1550 nm emission. Nano Lett. 19, 2418–2427.

Wei, W., Chen, G., Baev, A., He, G.S., Shao, W., Damasco, J., and Prasad, P.N. (2016). Alleviating luminescence concentration quenching in upconversion nanoparticles through organic dye sensitization. J. Am. Chem. Soc. 138, 15130–15133.

Wu, X., Zhang, Y., Takle, K., Bilsel, O., Li, Z., Lee, H., Zhang, Z., Li, D., Fan, W., Duan, C., et al. (2016). Dye-sensitized core/active shell upconversion nanoparticles for optogenetics and bioimaging applications. ACS Nano 10, 1060–1066.

Xiao, Y., Zeng, L., Xia, T., Wu, Z., and Liu, Z. (2015). Construction of an upconversion nanoprobe with few-atom silver nanoclusters as the energy acceptor. Angew. Chem. Int. Ed. 54, 5323–5327.

Ximendes, E.C., Santos, W.Q., Rocha, U., Kagola, U.K., Sanz-Rodriguez, F., Fernandez, N., Gouveia-Neto Ada, S., Bravo, D., Domingo, A.M., del Rosal, B., et al. (2016). Unveiling in vivo subcutaneous thermal dynamics by infrared luminescent nanothermometers. Nano Lett. 16, 1695–1703.

Ximendes, E.C., Rocha, U., Sales, T.O., Fernández, N., Sanz-Rodríguez, F., Martín, I.R., Jacinto, C., and Jaque, D. (2017). In vivo subcutaneous thermal video recording by supersensitive infrared nanothermometers. Adv. Funct. Mater. 27, 1702249.

Xu, J., Gulzar, A., Liu, Y., Bi, H., Gai, S., Liu, B., Yang, D., He, F., and Yang, P. (2017a). Integration of IR-808 sensitized upconversion nanostructure and MoS_2 nanosheet for 808 nm NIR light triggered phototherapy and bioimaging. Small 13, 1701841.

Xu, J., Yang, P., Sun, M., Bi, H., Liu, B., Yang, D., Gai, S., He, F., and Lin, J. (2017b). Highly emissive dye-sensitized upconversion nanostructure for dual-photosensitizer photodynamic therapy and bioimaging. ACS Nano 11, 4133–4144.

Xue, Z., Zeng, S., and Hao, J. (2018). Non-invasive through-skull brain vascular imaging and small

tumor diagnosis based on NIR-II emissive lanthanide nanoprobes beyond 1500 nm. Biomaterials *171*, 153–163.

Yamada, H., Arai, T., Endo, N., Yamashita, K., Fukuda, K., Sasada, M., and Uchiyama, T. (2006). LPS-induced ROS generation and changes in glutathione level and their relation to the maturation of human monocyte-derived dendritic cells. Life Sci. *78*, 926–933.

Yang, Q., Hu, Z., Zhu, S., Ma, R., Ma, H., Ma, Z., Wan, H., Zhu, T., Jiang, Z., Liu, W., et al. (2018). Donor engineering for NIR-II molecular fluorophores with enhanced fluorescent performance. J. Am. Chem. Soc. *140*, 1715–1724.

Yin, J., Kwon, Y., Kim, D., Lee, D., Kim, G., Hu, Y., Ryu, J.H., and Yoon, J. (2014). Cyanine-based fluorescent probe for highly selective detection of glutathione in cell cultures and live mouse tissues. J. Am. Chem. Soc. *136*, 5351–5358.

Zhang, H., Fan, Y., Pei, P., Sun, C., Lu, L., and Zhang, F. (2019a). Tm^{3+}-sensitized NIR-II fluorescent nanocrystals for *in vivo* information storage and decoding. Angew. Chem. Int. Ed. *58*, 10153–10157.

Zhang, M., Zheng, W., Liu, Y., Huang, P., Gong, Z., Wei, J., Gao, Y., Zhou, S., Li, X., and Chen, X. (2019b). A new class of blue-LED-excitable NIR-II luminescent nanoprobes based on lanthanide-doped CaS nanoparticles. Angew. Chem. Int. Ed. *58*, 9556–9560.

Zhang, X., Chen, W., Xie, X., Li, Y., Chen, D., Chao, Z., Liu, C., Ma, H., Liu, Y., and Ju, H. (2019c). Boosting luminance energy transfer efficiency in upconversion nanoparticles with an energy-concentrating zone. Angew. Chem. Int. Ed. *58*, 12117–12122.

Zhao, M., Li, B., Wang, P., Lu, L., Zhang, Z., Liu, L., Wang, S., Li, D., Wang, R., and Zhang, F. (2018). Supramolecularly engineered NIR-II and upconversion nanoparticles *in vivo* assembly and disassembly to improve bioimaging. Adv. Mater. *30*, 1804982.

Zhao, M., Wang, R., Li, B., Fan, Y., Wu, Y., Zhu, X., and Zhang, F. (2019). Precise *in vivo* inflammation imaging using in situ responsive cross-linking of glutathione-modified ultra-small NIR-II lanthanide nanoparticles. Angew. Chem. Int. Ed. *58*, 2050–2054.

Zou, W., Visser, C., Maduro, J.A., Pshenichnikov, M.S., and Hummelen, J.C. (2012). Broadband dye-sensitized upconversion of near-infrared light. Nat. Photonics *6*, 560–564.

Supplemental Information

A Universal Strategy to Construct Lanthanide-Doped Nanoparticles-Based Activable NIR-II Luminescence Probe for Bioimaging

Zhen Li, Junjie Wu, Qirong Wang, Tao Liang, Juan Ge, Peipei Wang, and Zhihong Liu

Supplemental Figures
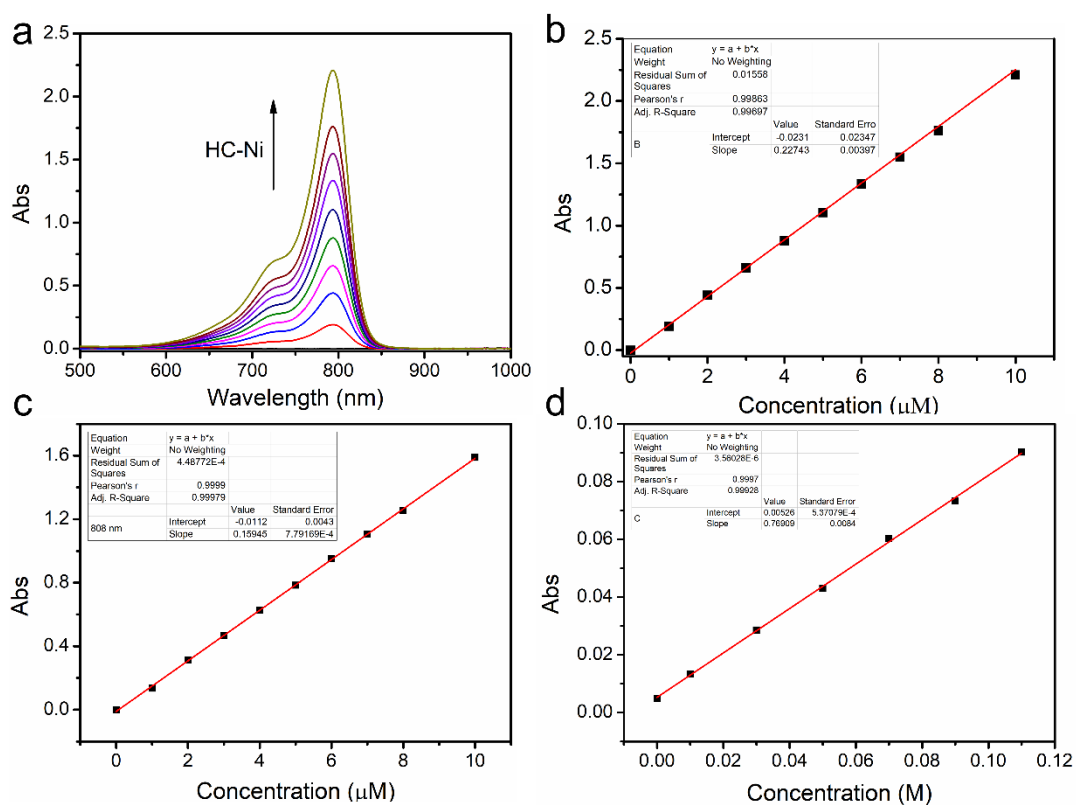
Figure S1. (a) The absorption spectra of **HC-Ni**. The molar absorption coefficient of **HC-Ni** at 794 nm (b) and 808 nm (c). The molar absorption coefficient of Nd^{3+} at 808 nm (d). Related to Figure 1.
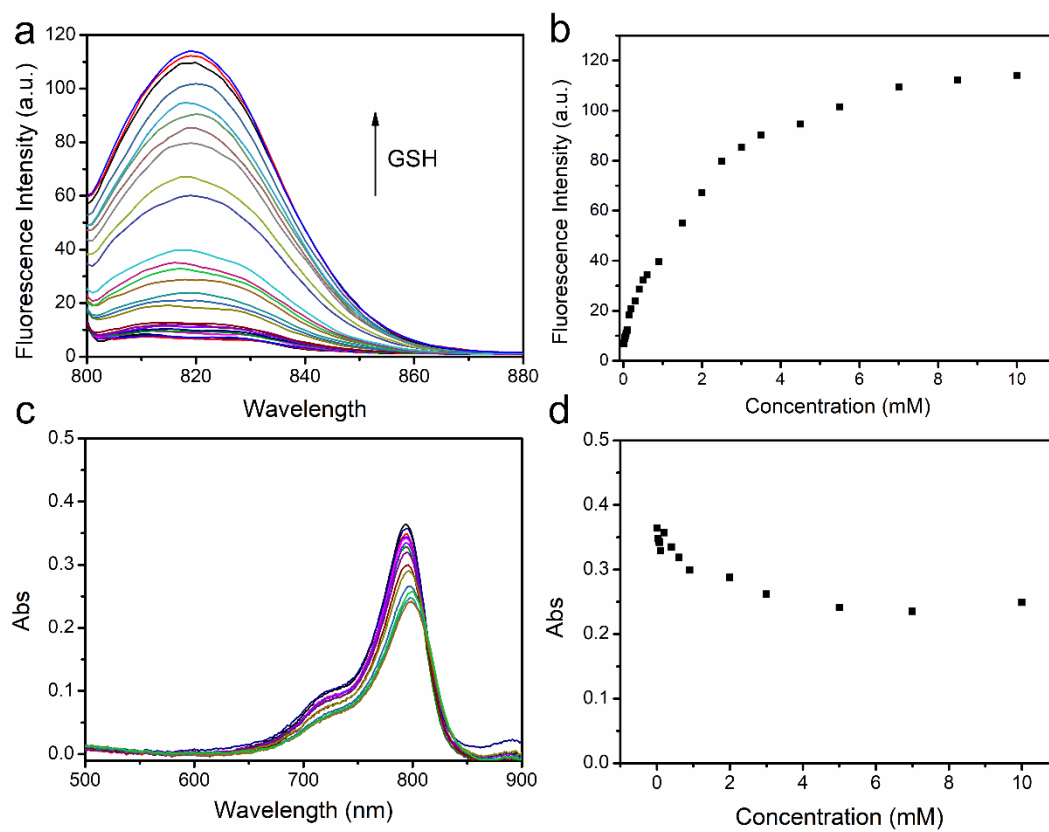
Figure S2. Fluorescence emission spectra (a) and UV-vis absorption spectra (c) of **HC-Ni** excited with 780 nm after reacting with various concentrations of GSH in the mixture solvent of DMSO and HEPES (100 mM, pH 7.2, v:v=1:1). Dependence of the emission intensity at 820 nm (b) and absorbance at 794 nm (d) on the concentration of GSH. Related to Figure 1.
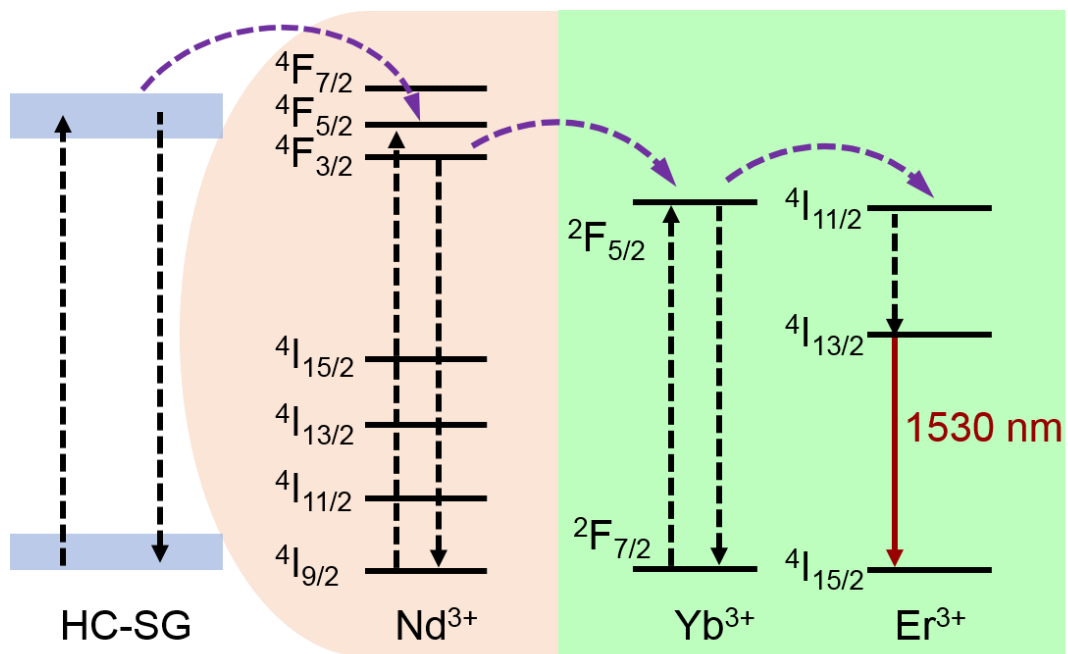
Figure S3. Schematic illustration of the energy transfer process from HC-SG to LnNPs. Related to Figure 2.
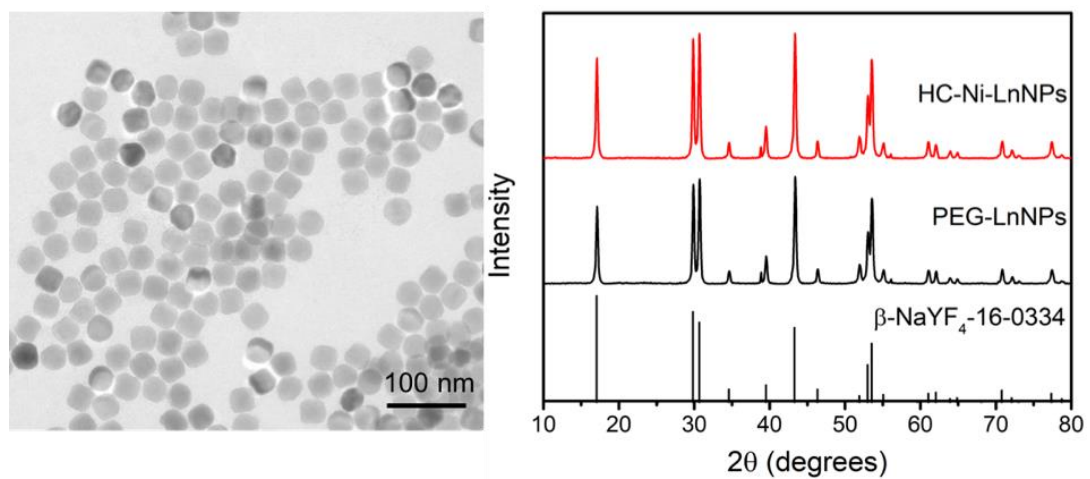
Figure S4. (a) TEM image of HC-Ni-LnNPs. (b) XRD patterns of HC-Ni-LnNPs and DSPE-PEG coated LnNPs (termed as PEG-LnNPs). Related to Figure 2.
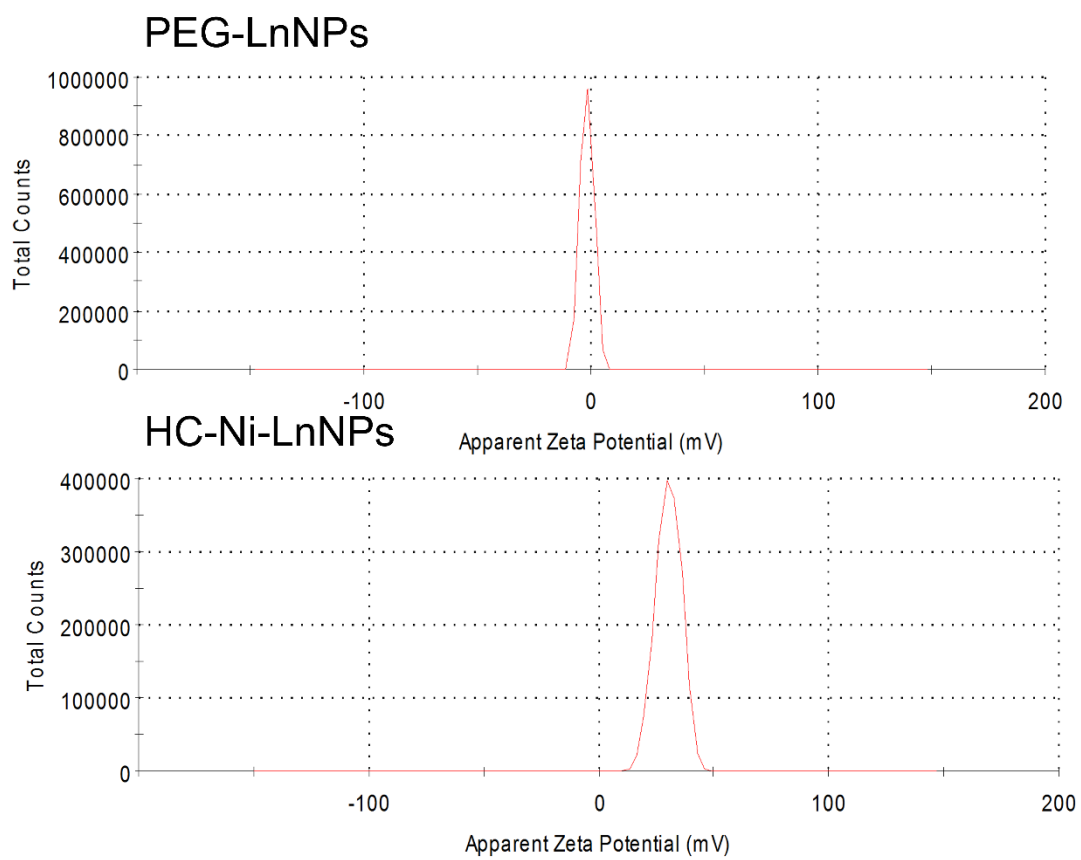
Figure S5. ζ potential of HC-Ni-LnNPs and PEG-LnNPs. Related to Figure 2.

	core	10%	20%	30%	40%	50%

33.9±1.4nm   37.9±1.5nm   37.0±1.6nm   37.6±1.6nm   37.3±1.6nm   37.6±1.8nm
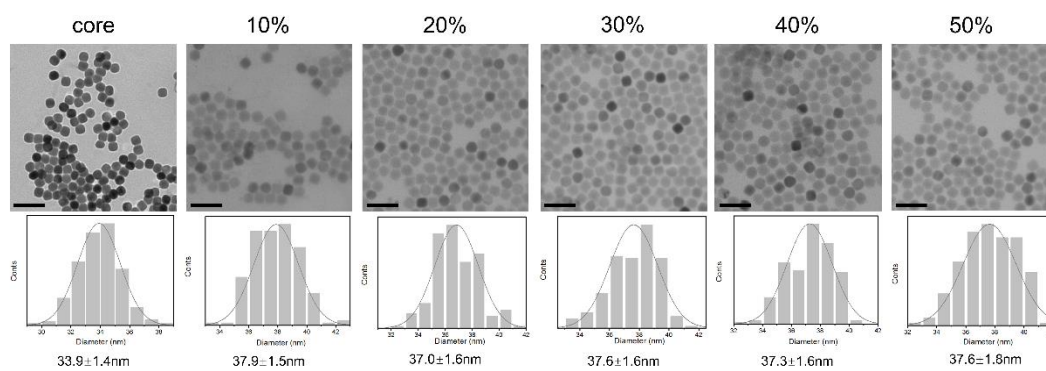
Figure S6. TEM images and histograms of the size distribution of the core-structured LnNPs and core-shell LnNPs with doping different concentrations of Nd^{3+} in the shell. Scale bar: 100 nm. Related to Figure 3.
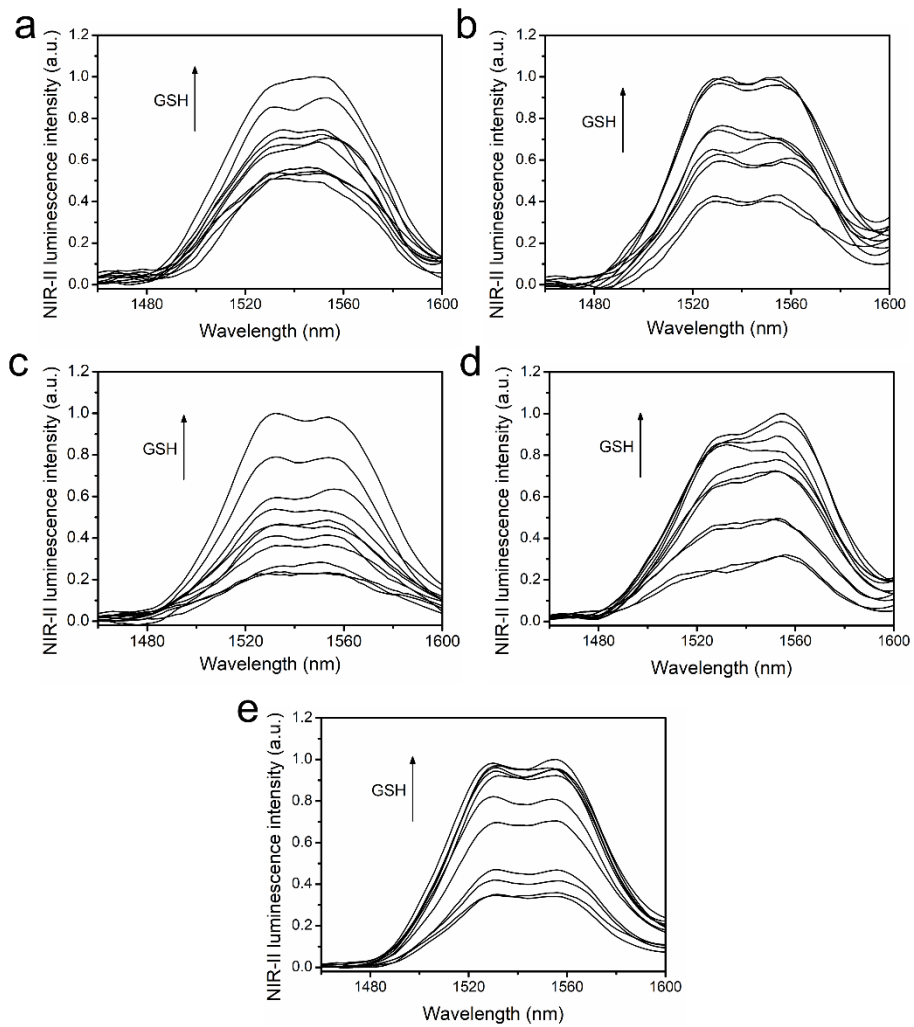
Figure S7. NIR-II luminescence spectra of HC-Ni-UCNPs responding to GSH with different Nd^{3+} doping concentrations in the shell (a: 10%; b: 20%; c: 30%; d: 40%; e: 50%). Related to Figure 3.

37.8±1.9nm 40.1±1.7nm 41.7±2.3nm 45.2±2.2nm
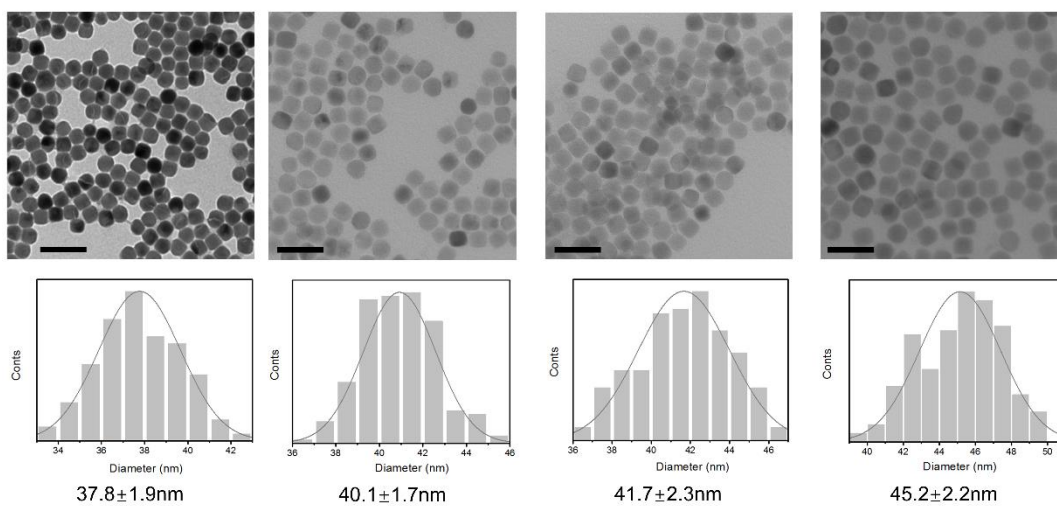
Figure S8. TEM images and histograms of the size distribution of the core-shell LnNPs with different thickness of the shell. Scale bar: 100 nm. Related to Figure 3.
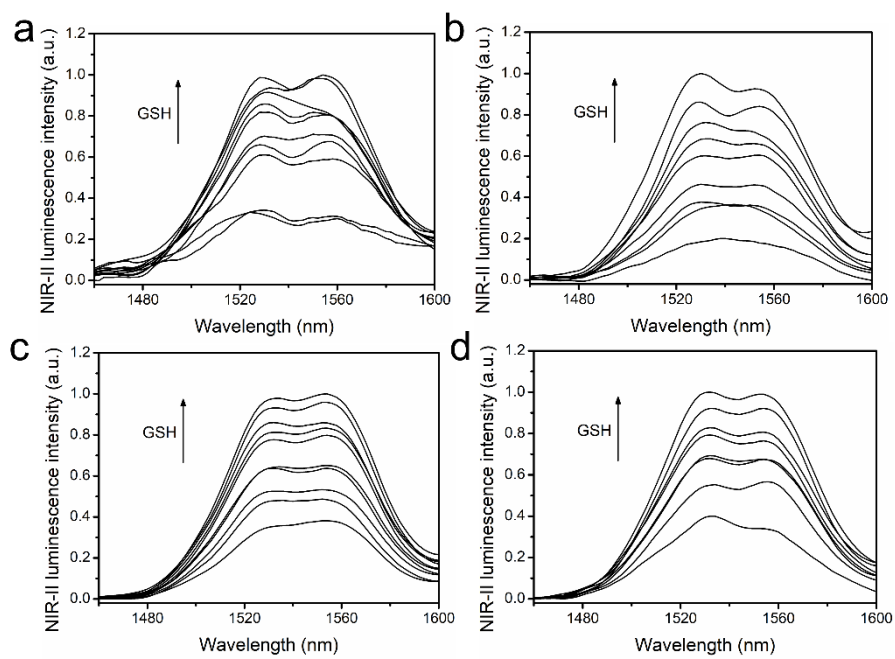
Figure S9. NIR-II luminescence spectra of HC-Ni-UCNPs responding to GSH with various shell thickness of LnNPs (a: 1.9 nm; b: 3.1 nm; c: 3.9 nm; d: 5.6 nm). Related to Figure 3.
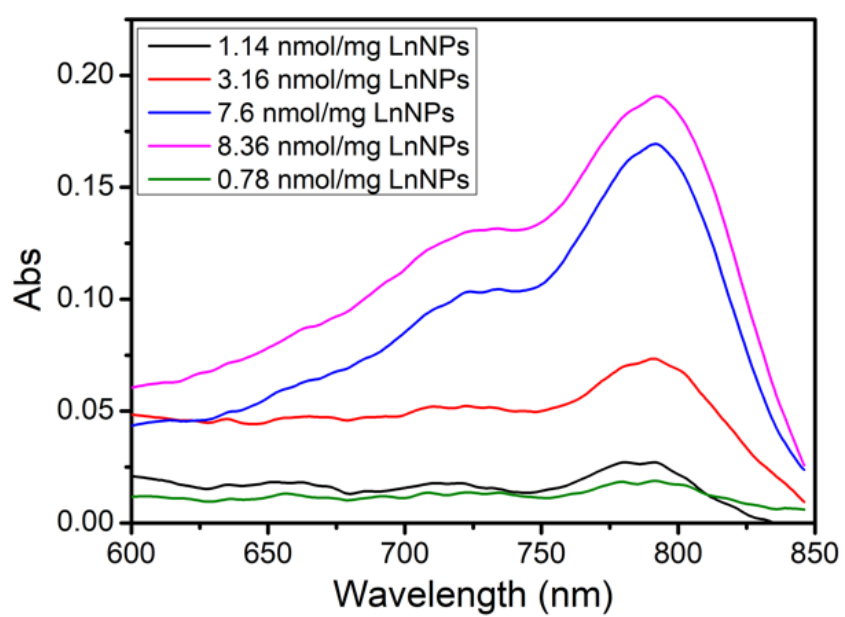
Figure S10. UV-vis spectra of 0.1 mg/mL HC-Ni-LnNPs assembled with various concentrations of **HC-Ni**. Related to Figure 3.
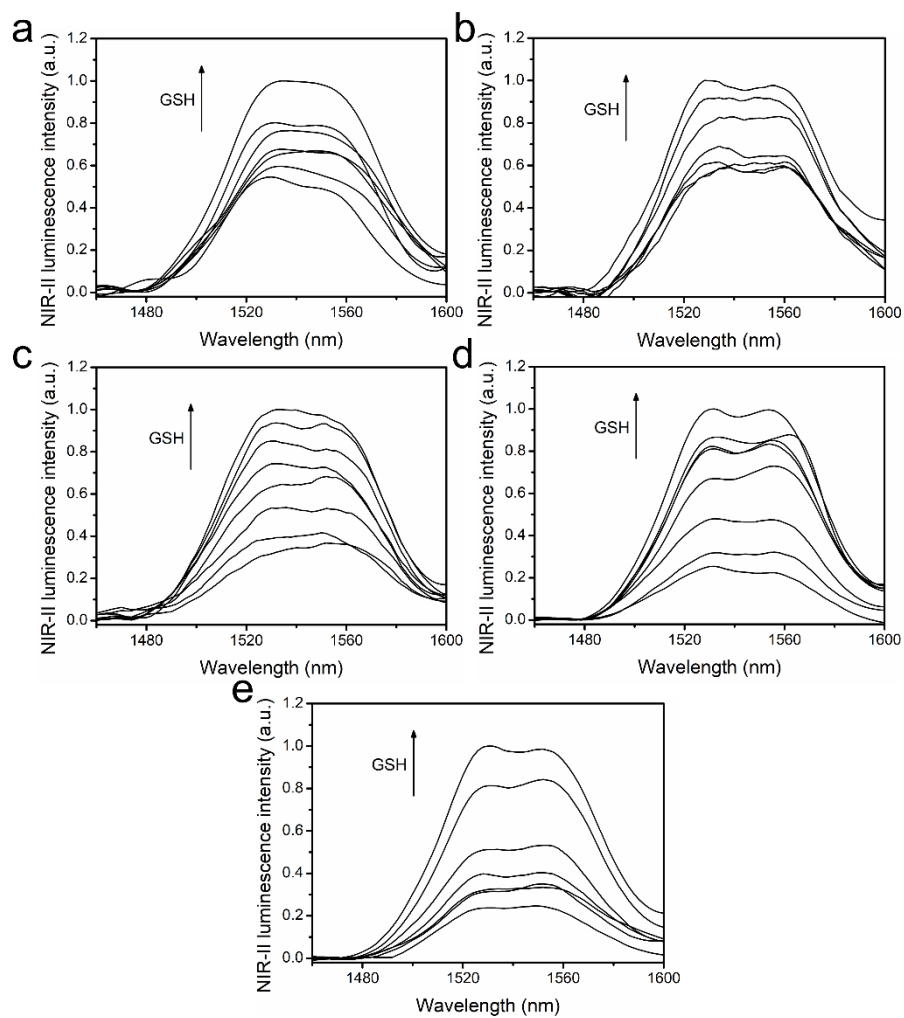
Figure S11. NIR-II luminescence spectra of HC-Ni-UCNPs responding to GSH with different loading capacity of **HC-Ni** (a: 0.78 nmol/mg LnNPs; b: 1.4 nmol/mg LnNPs; c: 3.16 nmol/mg LnNPs; d: 7.6 nmol/mg LnNPs; e: 8.36 nmol/mg LnNPs). Related to Figure 3.
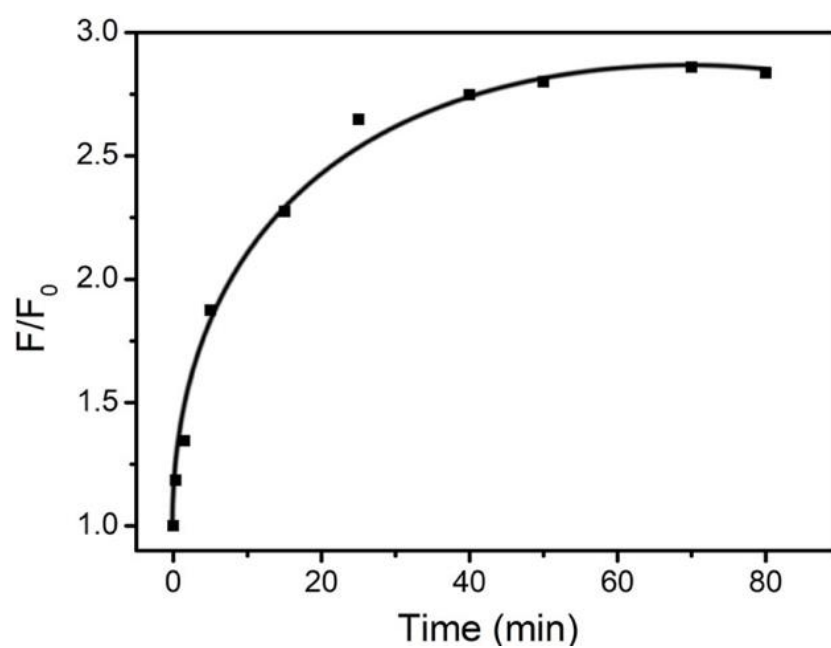
Figure S12. Dependence of the NIR-II luminescence intensity at 1530 nm of HC-Ni-LnNPs on the time of reaction with GSH, with the GSH concentration fixed. Related to Figure 3.
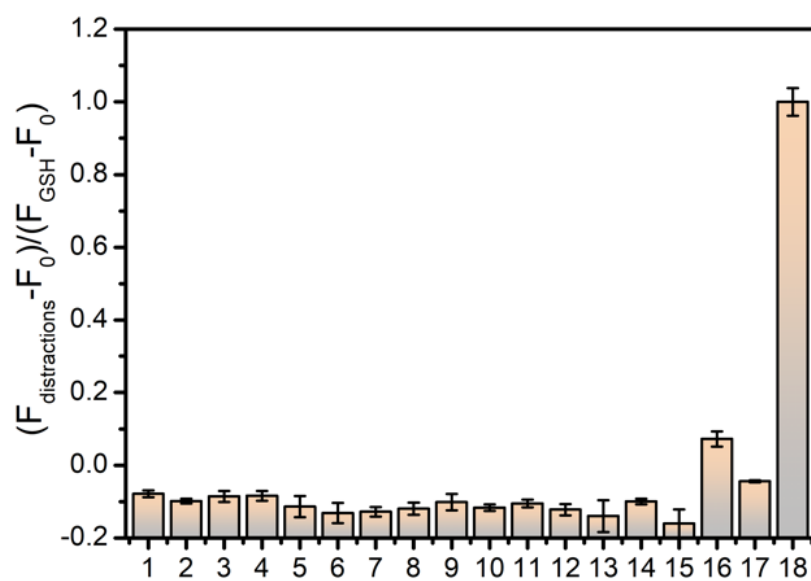
Figure S13. Selectivity of the HC-Ni-LnNPs to GSH against other disruptors (1: NaCl; 2: KCl; 3: CaCl$_2$; 4: glucose; 5: Pro; 6: Ala; 7: Met; 8: His; 9: Lys; 10: Ser; 11: Val; 12: ClO$^-$; 13: H$_2$O$_2$; 14: KO$_2$; 15: Na$_2$S; 16: Hcy; 17: Cys; 18: GSH). The concentration of all tested species was 1 mM. Data are represented as mean±SD (n=3). Related to Figure 3.
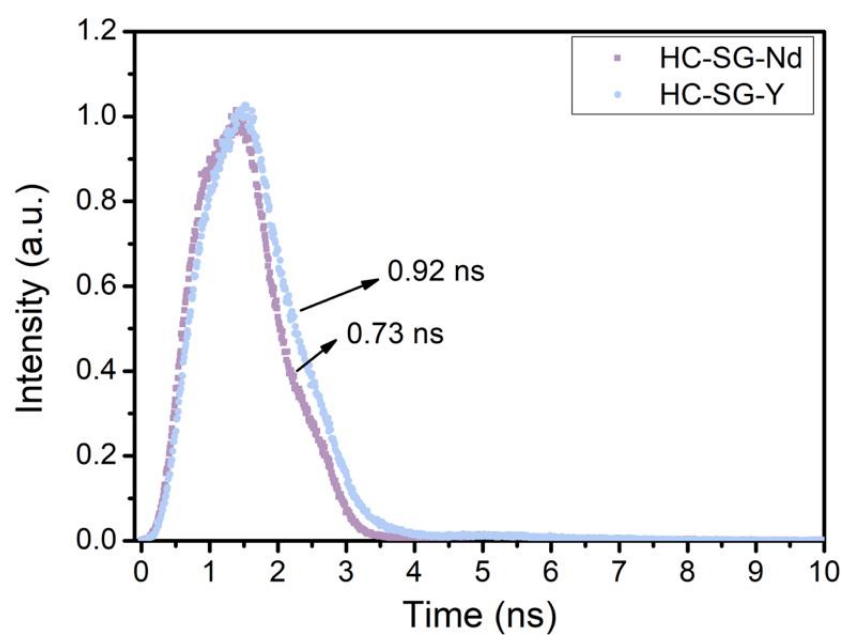
Figure S14. Time-resolved fluorescence spectra of **HC-SG** assembled on the surface of nanoparticles with or without doping Nd^{3+}. Related to Figure 3.
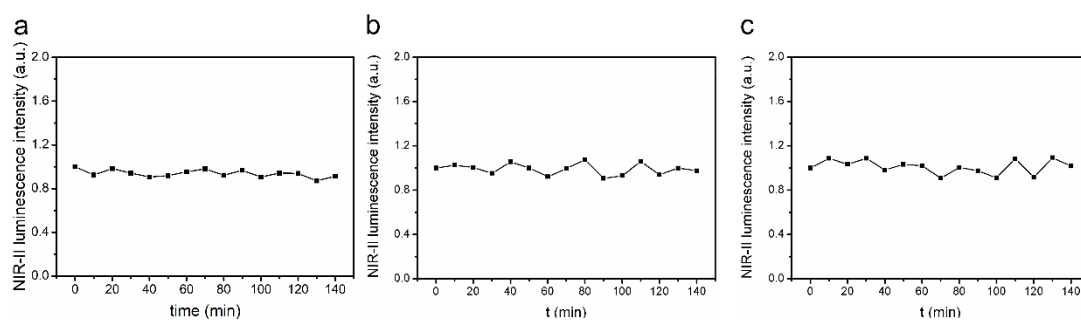
Figure S15. The NIR-II luminescence intensity of HC-Ni-LnNPs after incubation at 37 °C in (a) HEPES, (b) FBS and (c) DMEM for different time. Related to Figure 4.
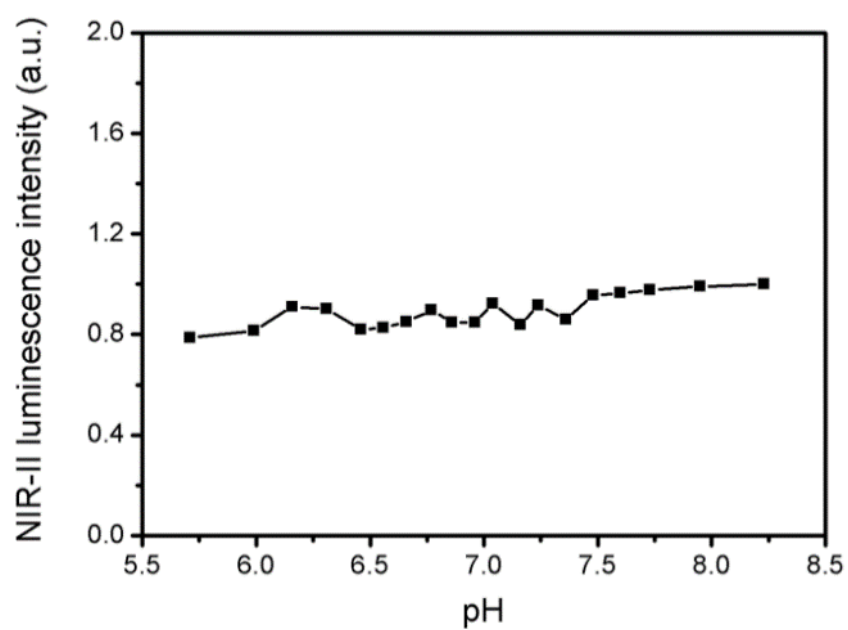
Figure S16. The NIR-II luminescence intensity of HC-Ni-LnNPs after incubation at 37 °C at different pH. Related to Figure 4.
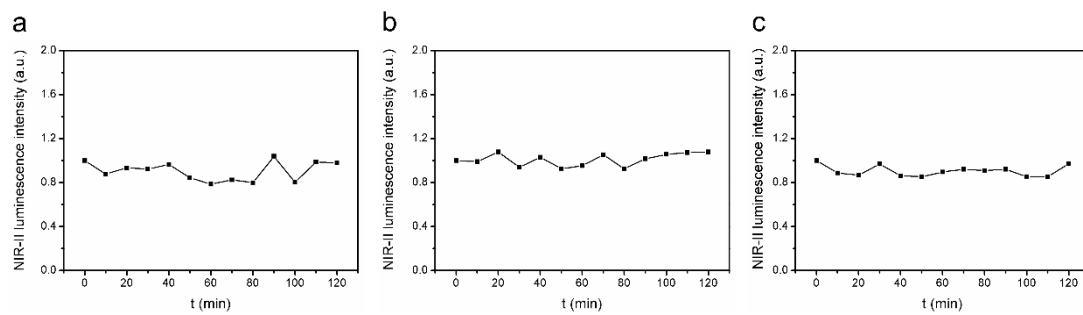
Figure S17. The NIR-II luminescence intensity of HC-SG-LnNPs after incubation at 37 °C in (a) HEPES, (b) FBS and (c) DMEM for different time. Related to Figure 4.
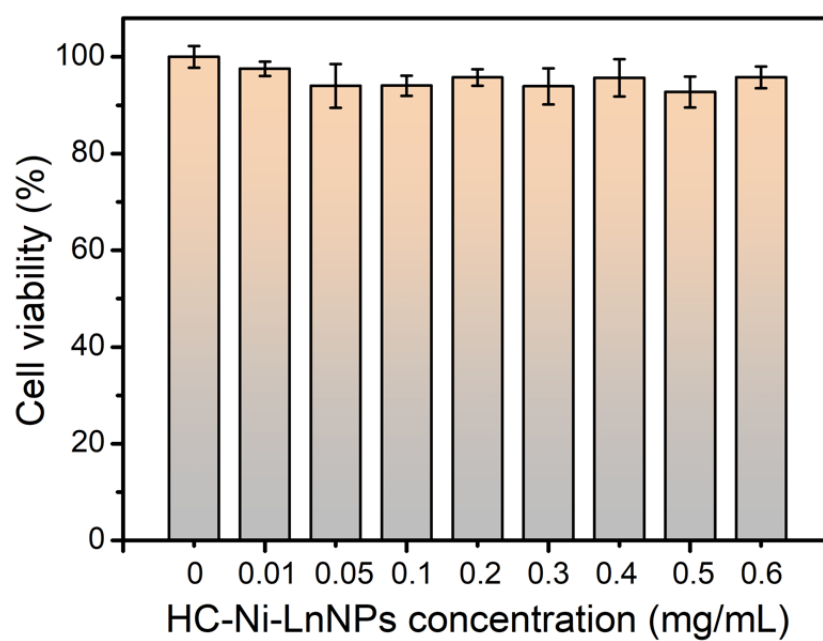
Figure S18. Cell viability of 4T1 cells incubated with different concentrations of HC-Ni-LnNPs at 37 °C for 24 h. Data are represented as mean±SD (n=6). Related to Figure 4.
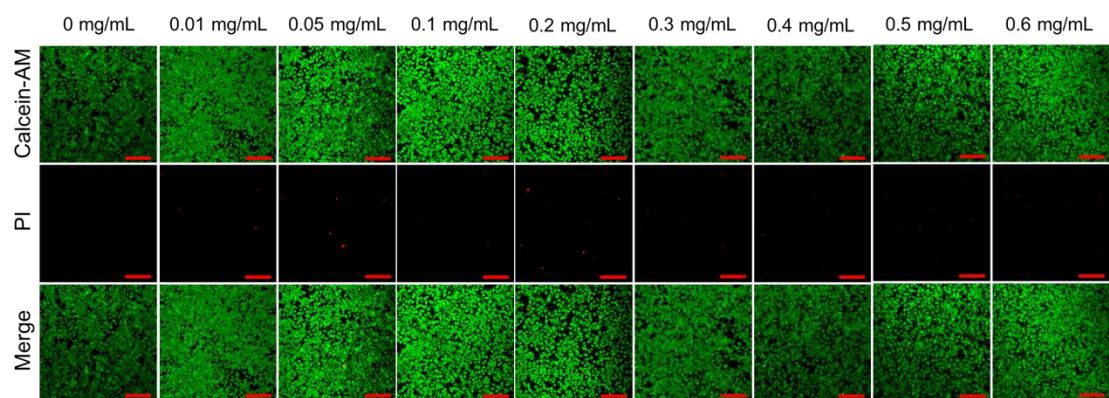
Figure S19. Confocal images of calcein-AM and PI co-stained 4T1 cells incubated with different concentrations of HC-Ni-LnNPs at 37 °C for 24 h. Scale bar: 200 µm. Related to Figure 4.
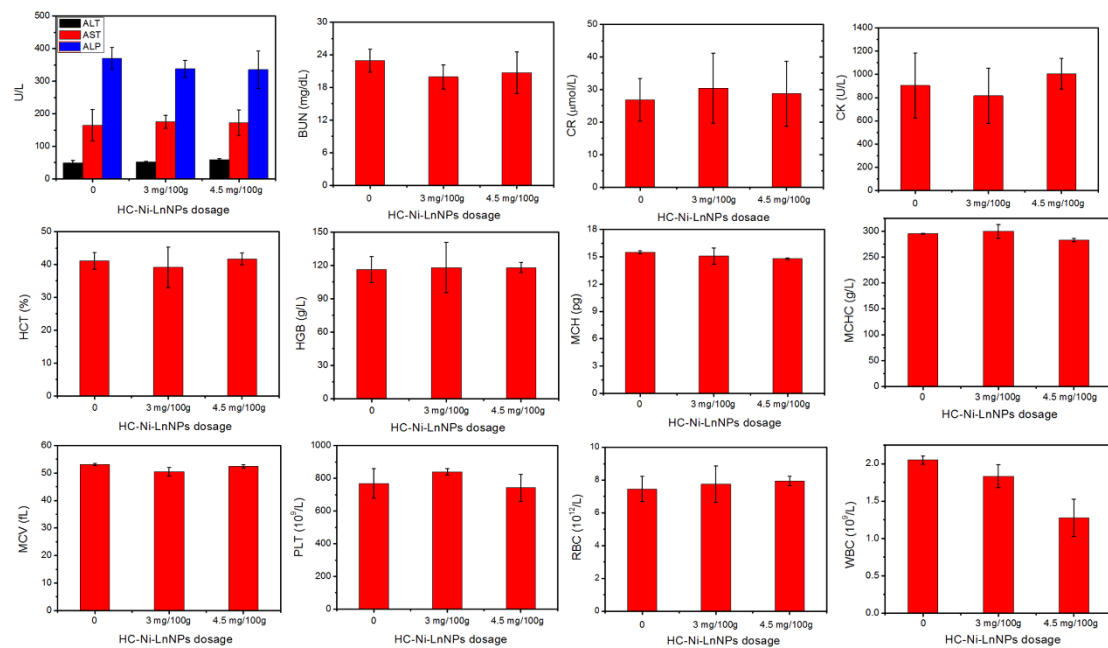
Figure S20. Blood routine and serum biochemical levels of mice after receiving different doses of HC-Ni-LnNPs, including alanine aminotransferase (ALT), aspartate aminotransferase (AST), alkaline phosphatase (ALP), blood urea nitrogen (BUN), creatinine (CR), Creatine Kinase (CK), hematocrit (HCT), hemoglobin (HGB), mean corpuscular hemoglobin (MCH), mean corpuscular hemoglobin concentration (MCHC), mean corpuscular volume (MCV), platelet (PLT), red blood count (RBC) and white blood count (WBC). Data are represented as mean±SD (n=3). Related to Figure 4.
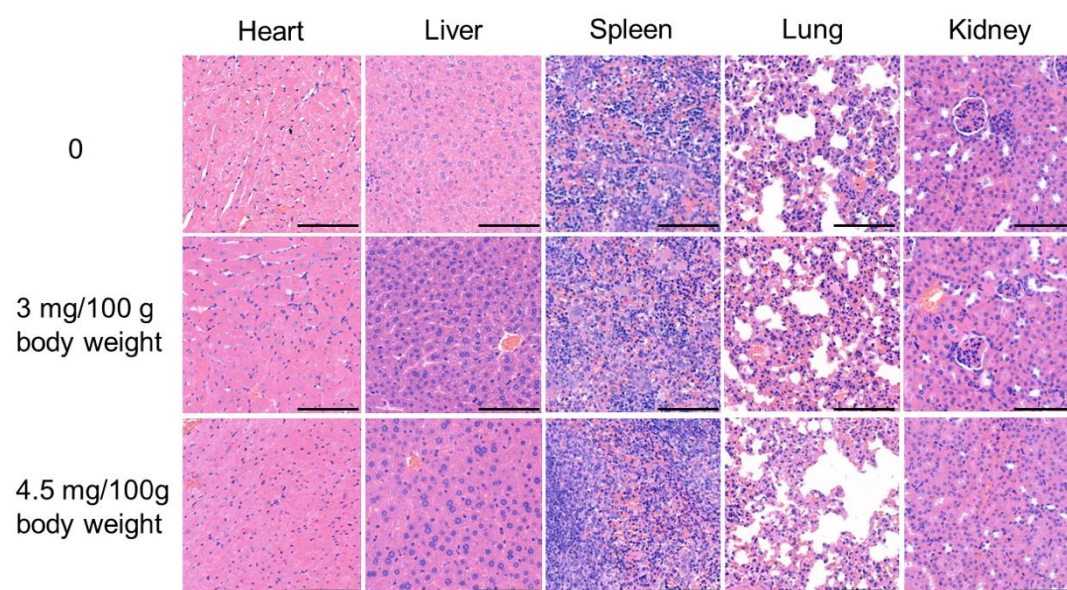
Figure S21. H&E staining images of major mice organs after tail vein injection of various dosages of HC-Ni-LnNPs for 7 days. Scale bar: 100 µm. Related to Figure 4.
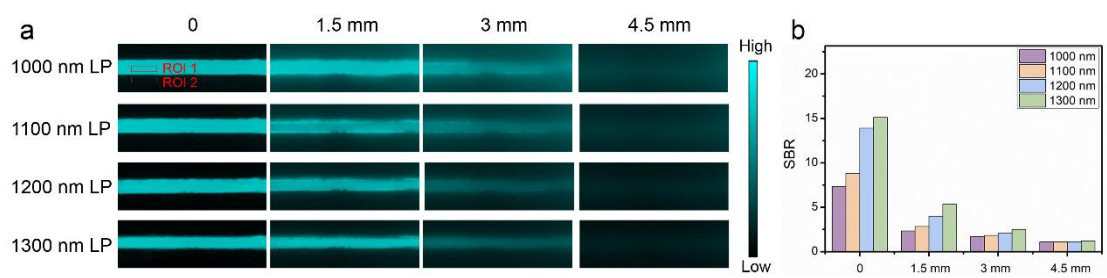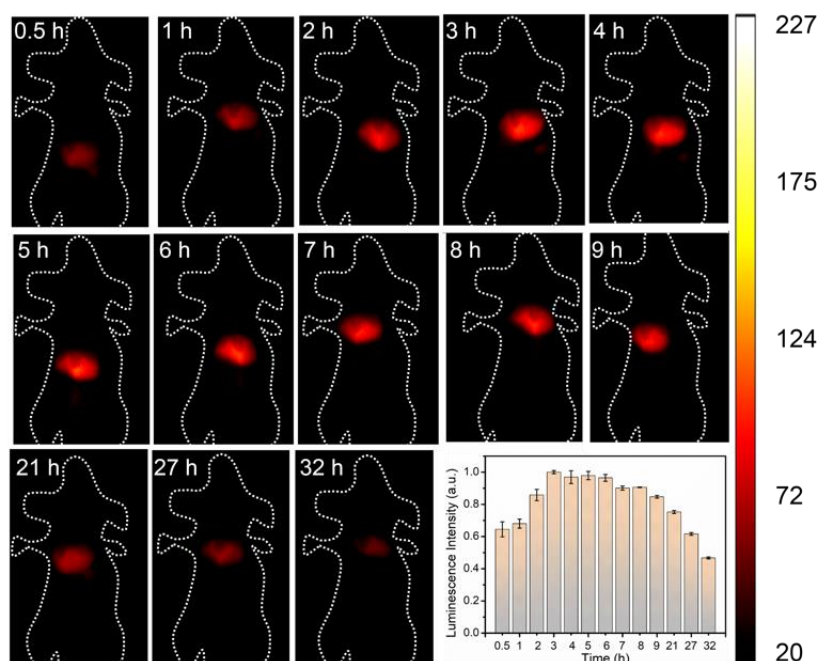
Figure S22. (a) Wavelength-dependent NIR-II luminescence of cuvette covered with different thicknesses of lard. (b) SBR (defined as ROI1/ROI2) obtained for different wavelengths at various depths. Related to Figure 4.
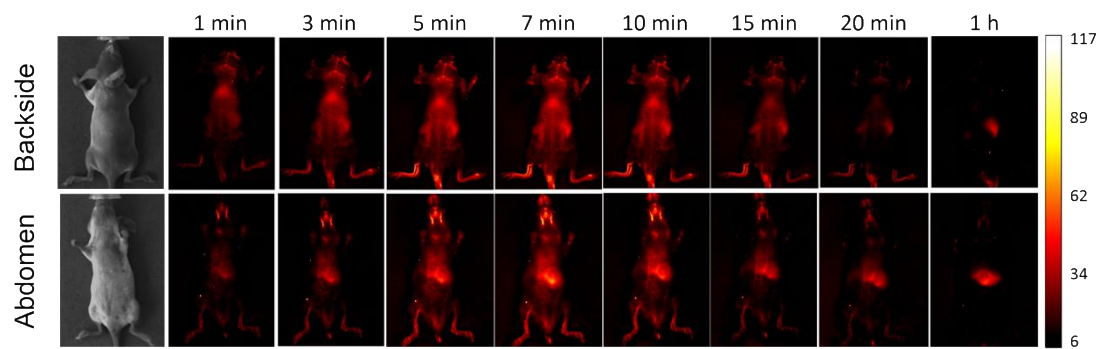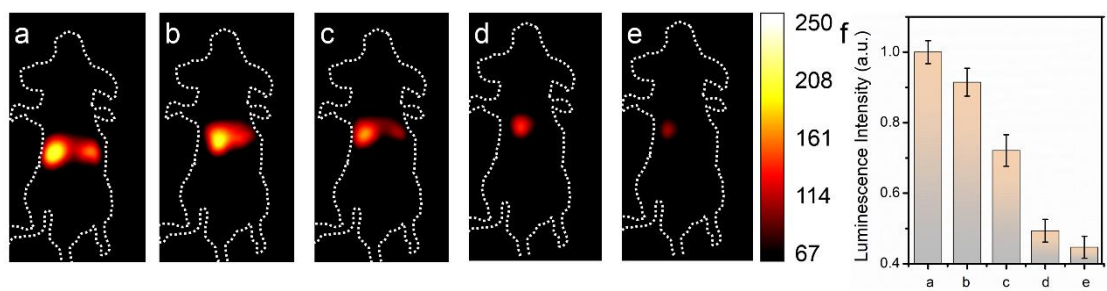
Figure S23. *In vivo* NIR-II luminescence imaging of HC-Ni-LnNPs at different time points after i.v. injection. Related to Figure 4.
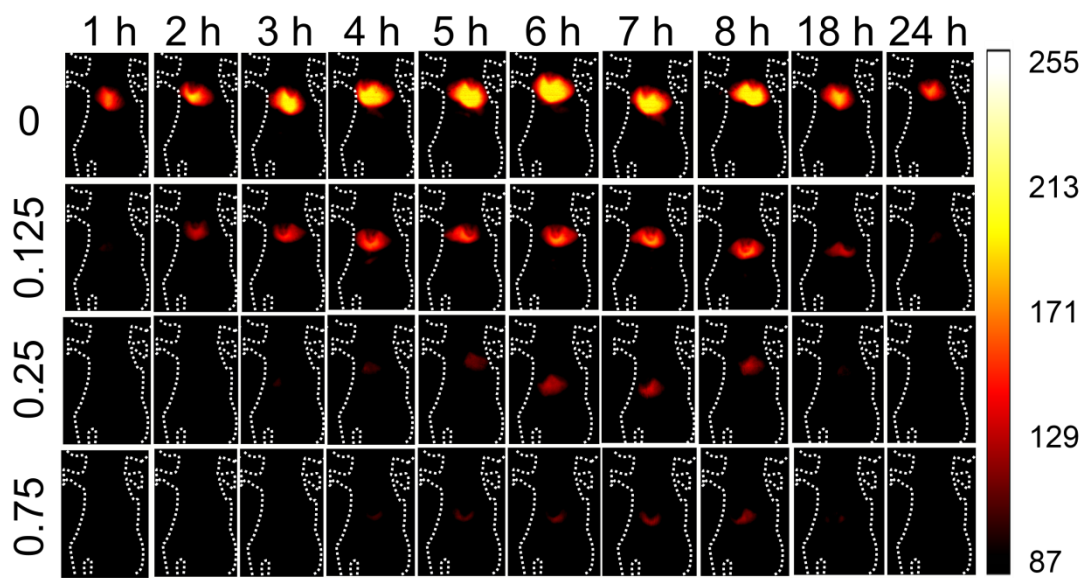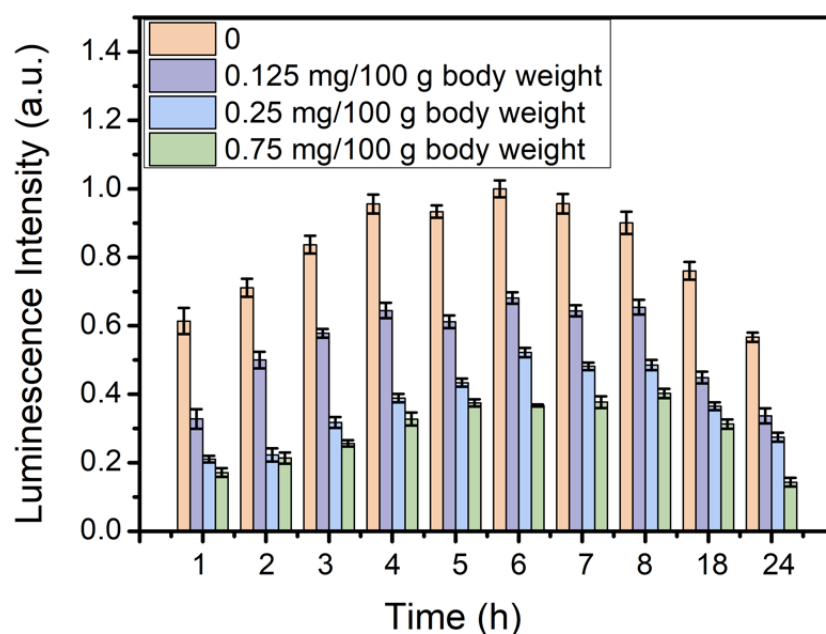
Figure S24. *In vivo* NIR-II luminescence imaging of HC-Ni-LnNPs in liver at different time points after i.v. injection. Data are represented as mean±SD (n=3). Related to Figure 4.

Figure S25. *In vivo* NIR-II luminescence imaging of mice injected with NMM (a: 0, b: 0.5, c: 1, d: 1.5, e: 2 mg/ 100 g body weight) 0.5 h before the injection of HC-Ni-LnNPs. Data are represented as mean±SD (n=3). Related to Figure 4.

Figure S26. *In vivo* NIR-II luminescence imaging of mice injected with LPS (a: 0, b: 0.125, c: 0.25, d: 0.75 mg/100 g body wight) 24 h before the injection of HC-Ni-LnNPs. The images were recorded at different time points. Related to Figure 4.

Figure S27. NIR-II luminescence intensities of mice injected with LPS (0, 0.125, 0.25 and 0.75 mg/ 100 g body weight) 24 h before the injection of HC-Ni-LnNPs at different time points. Data are represented as mean±SD (n=3). Related to Figure 4.
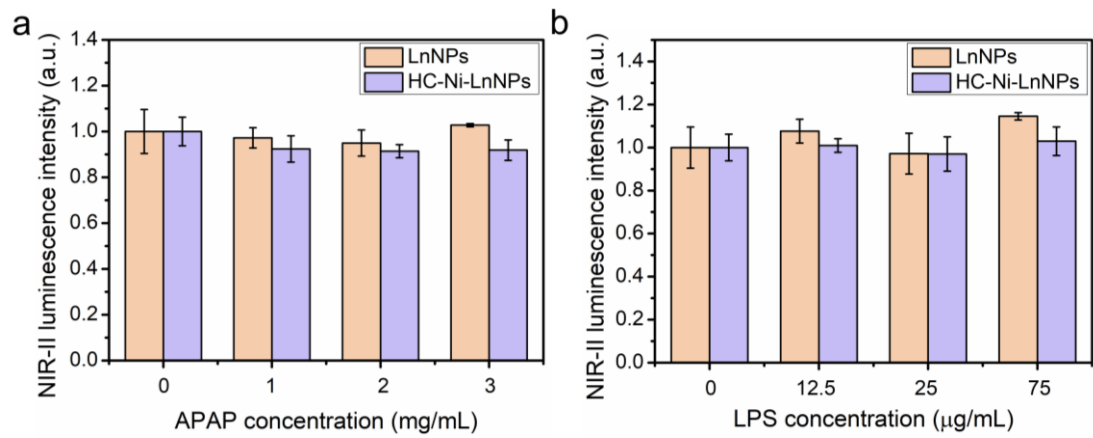
Figure S28. NIR-II luminescence intensity of LnNPs or HC-Ni-LnNPs incubated with a) APAP or b) LPS with different concentrations. Data are represented as mean±SD (n=3). Related to Figure 4.
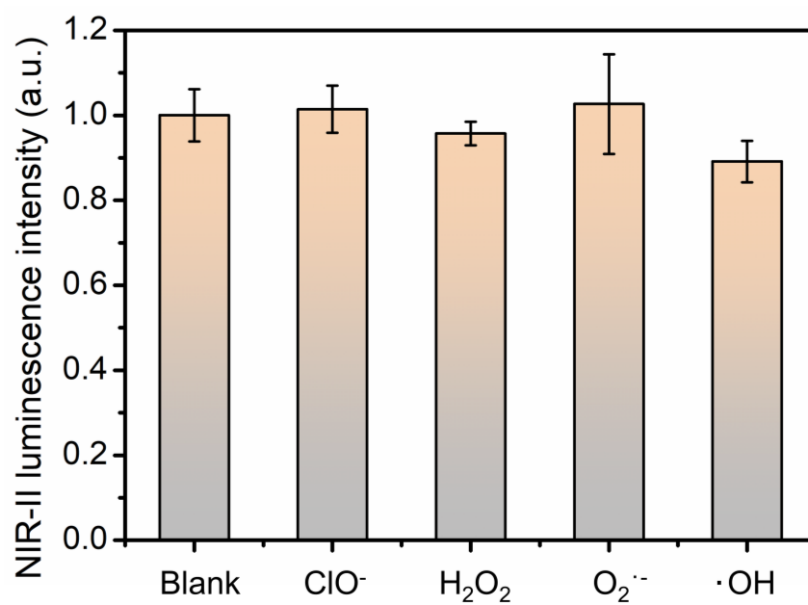
Figure S29. NIR-II luminescence intensity of HC-SG-LnNPs incubated with ROS. Data are represented as mean±SD (n=3). Related to Figure 4.
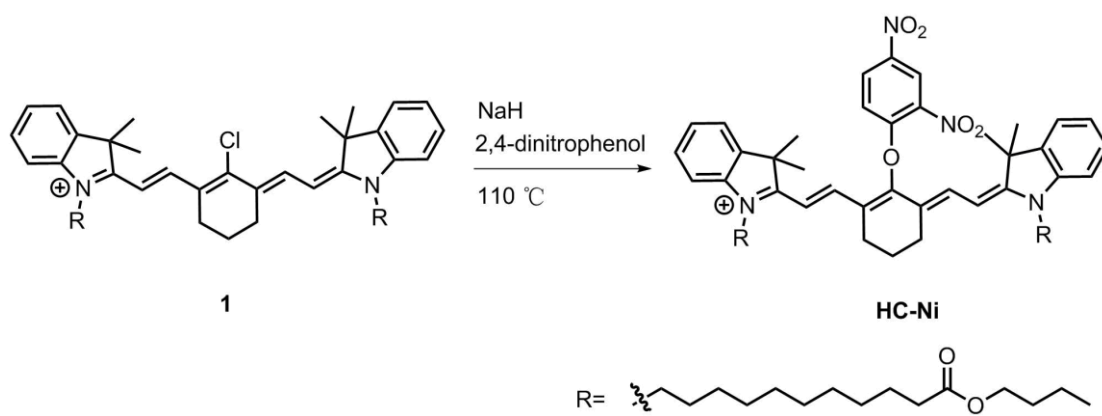
Figure S30. Synthetic route of **HC-Ni**. Related to Scheme 1.

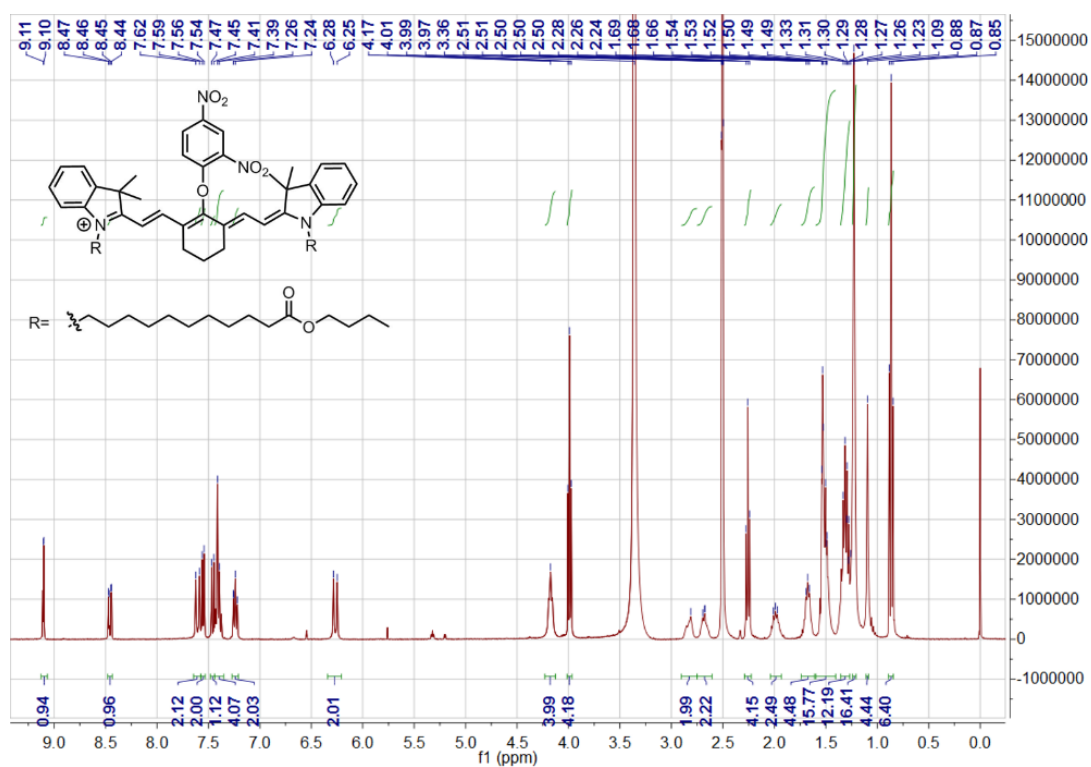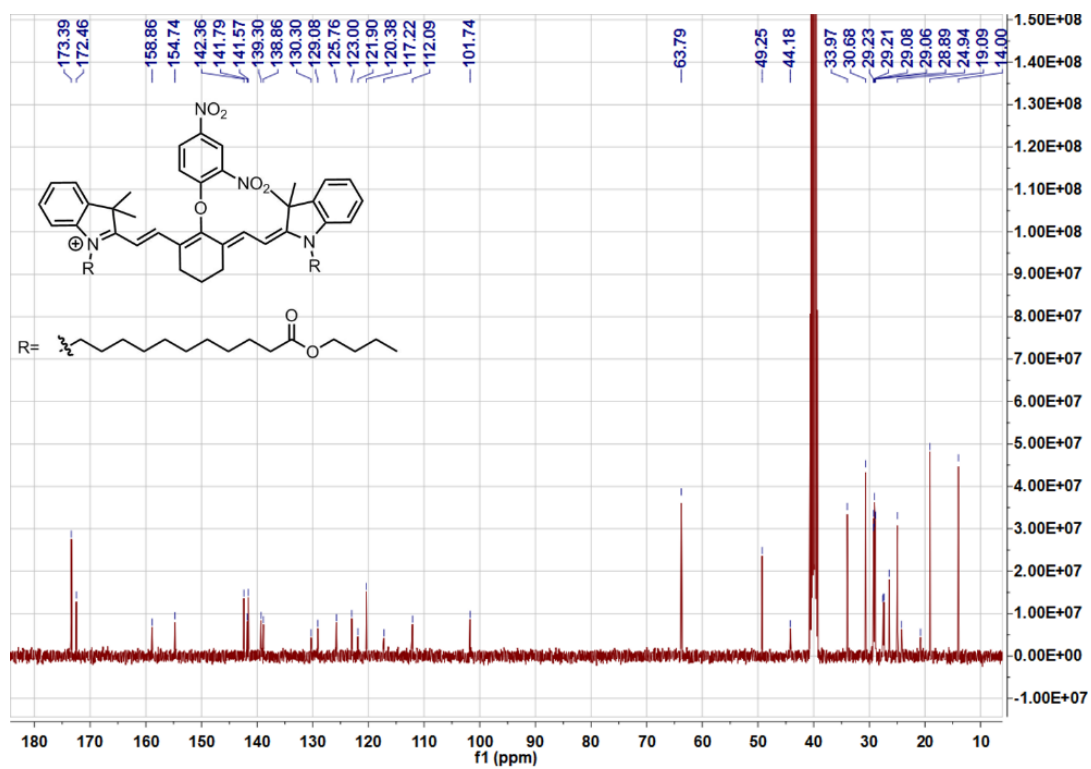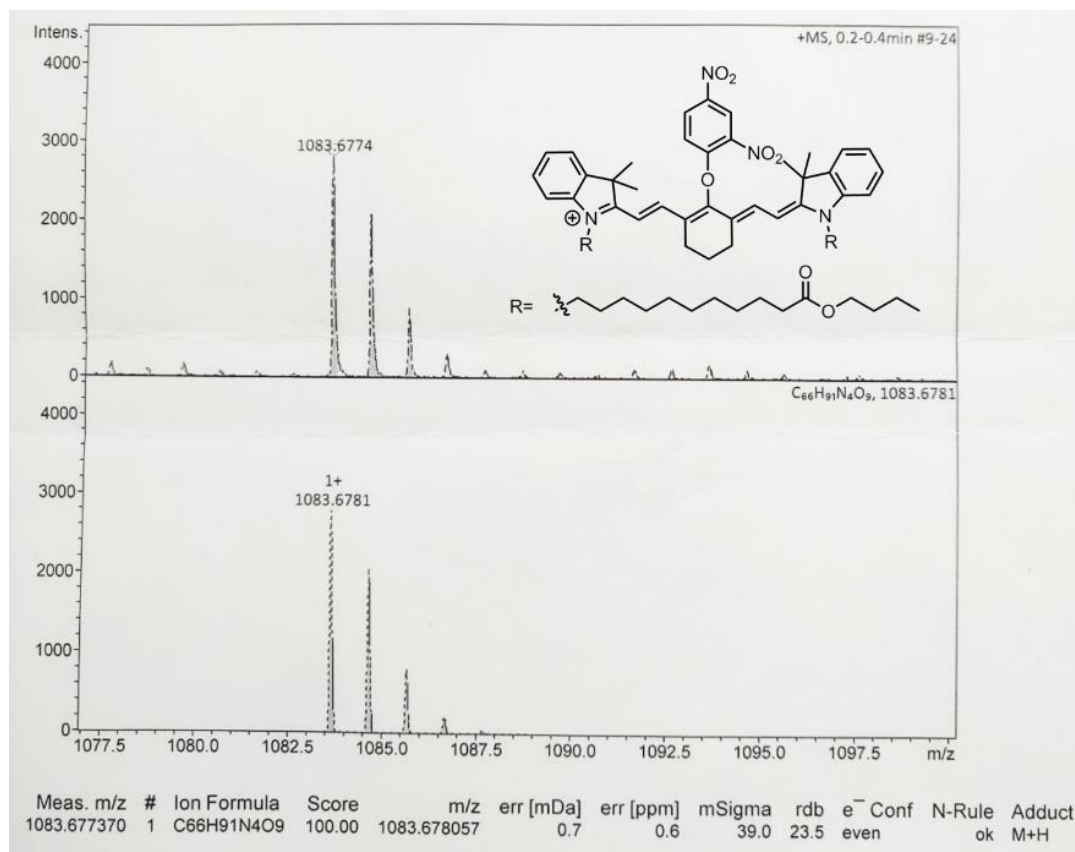**Figure S31.** ^{1}H NMR spectrum of **HC-Ni**. Related to Scheme 1.

Figure S32. ^{13}C NMR spectrum of **HC-Ni**. Related to Scheme 1.

Figure S33. High resolution mass spectrum (HRMS) of **HC-Ni**. Related to Scheme 1.

Materials and instruments

1-Octadecene, oleic acid, Ln_2O_3, 3-iodopropionic acid, 2,3,3-trimethylindolenine and 11-bromoundecanoic acid were obtained from Aladdin Reagent, Ltd. (Shanghai, China). DSPE-PEG was purchased from Xi'an ruixi Biological Technology Co., Ltd. Other chemical reagents were supplied by Sinopharm Chemical Reagent Co., Ltd. (Shanghai, China). The reagents were all analytical or higher grade, and used without further purification. All aqueous solutions were prepared using ultrapure water (Mill-Q, Millipore, 18.2 MΩ resistivity). Mice were provided by Wuhan Goodbio technology Co. Ltd. (Wuhan, China). All animal studies were performed in accordance with Animal Care and Use Committee of Wuhan University.

The morphology and size of LnNPs were acquired by a JEM-2010 transmission electron microscope (TEM) operated at 200 kV. The crystal phase was characterized using an X-ray diffractometer (XRD, Bruker D8 Discover) with a 2θ range of 10°-80° with Cu Kα irradiation (k=1.5406 Å). FT-IR spectra measurements were acquired on Nicolet 5700 FTIR Spectrometer (Thermo Fisher Scientific, USA). NIR-II fluorescence spectra were excited by 808-nm laser and measured with a fluorometer (FLS1000, Edinburgh Instrument). UV-vis spectra were recorded by a UV 2550 UV-vis spectrophotometer (Shimadzu, Japan). MTT test was detected by Mk3 microplate reader (Thermo Scientific Multiskan, USA). Fluorescence microscopy images of 4T1 cells were conducted on Zeiss LSM 880 Microscope. *In vivo* NIR-II luminescence images were acquired by In-Vivo Master NIR-II luminescence imaging system (Grand Imaging Technology Co. Ltd., Wuhan).

Transparent Methods

Synthesis of HC-Ni. 4.8 mg NaH with a mass fraction of 60% (0.12 mmol) was added into 2,4-dinitrophenol (22 mg, 0.12 mmol) in 10 mL anhydrous DMF. The mixture was stirred at room temperature for 30 min. 100 mg compound 1 (Liang et al., 2018) (0.10 mmol) was then added and stirred overnight at 70 °C. After cooled to room temperature, the reaction system was poured into 100 mL NaCl saturated solution and then extracted with ethyl acetate. The organic layer was evaporated and the crude product was purified by column chromatography on silica gel with gradient CH_2Cl_2 to CH_2Cl_2/MeOH =10:1 (v:v) eluent to obtain **HC-Ni** as dark green solid (15 mg, 14% yield). ^1H NMR (400 MHz, DMSO) δ 9.10 (d, J = 2.8 Hz, 1H), 8.46 (dd, J = 9.3, 2.8 Hz, 1H), 7.60 (d, J = 14.1 Hz, 2H), 7.55 (d, J = 7.4 Hz, 2H), 7.46 (d, J = 9.3 Hz, 1H), 7.40 (d, J = 6.8 Hz, 4H), 7.24 (dd, J = 10.8, 4.9 Hz, 2H), 6.27 (d, J = 14.3 Hz, 2H), 4.17 (s, 4H), 3.99 (t, J = 6.6 Hz, 4H), 2.81 (s, 2H), 2.75-2.60 (m, 2H), 2.26 (t, J = 7.3 Hz, 4H), 2.05-1.93 (m, 2H), 1.74-1.61 (m, 4H), 1.60-1.41 (m, 16H), 1.36-1.27 (m, 12H), 1.23 (m, 16H), 1.09 (s, 4H), 0.87 (t, J = 7.4 Hz, 6H). ^{13}C NMR (101 MHz, DMSO) δ 173.39, 172.46, 158.86, 154.74, 142.36, 141.79, 141.57, 139.30, 138.86, 130.30, 129.08, 125.76, 123.00, 121.90, 120.38, 117.22, 112.09, 101.74, 63.79, 49.25, 44.18, 33.97, 30.68, 29.23, 29.21, 29.08, 29.06, 28.89, 27.56, 27.47, 27.37, 26.44, 24.94, 24.22, 20.80, 19.09, 14.00. HRMS (ESI) for $C_{66}H_{91}N_4O_9$ $[M]^+$: calcd 1083.6781, found 1083.6774.

Synthesis of OA-LnNPs. 1 mmol $Ln(oleate)_3$ ($Er^{3+}:Yb^{3+}:Y^{3+}$ = 2:20:78) and 20 mmol NaF were added to the mixed solvent of 10 mL oleic acid and 10 ml 1-octadecene and then degassed for 1 h at 110 °C. The mixture was heated to 320 °C for about 2.5 h to obtain the core structured LnNPs. 4 mL of the mixture was acquired for characterization. The shell layer was then grown on the core by injection of various amounts of $Ln(oleate)_3$, which were consisted of $Y(oleate)_3$ and $Nd(oleate)_3$ with different ratios. After reaction at 320 °C for another 1 h, the reaction system was cooled to room temperature. The OA-LnNPs was precipitated after addition of equal volume of EtOH and then washed by hexane/EtOH (v:v = 1:1) for three times. The obtained OA-LnNPs was finally dispersed in hexane.

Preparation of HC-Ni-LnNPs Nanoprobe. OA-LnNPs (1 mg/mL) in $CHCl_3$ was added with equal mass of DSPE-PEG. The solvent was evaporated under nitrogen atmosphere and then the solid was dispersed in water with a concentration of 1 mg/mL. Different volumes of **HC-Ni** (10 mM in DMSO) were added to the mixture and kept vigorously shaking for about 1 min. Free **HC-Ni** was then removed though centrifugation at a speed of 13000 r/min for 18 min. The precipitation was washed twice with water and finally dispersed in water (1 mg/mL).

Luminescence Response of HC-Ni-LnNPs to GSH. This experiment was conducted in 100 mM HEPES (pH=7.2) at 37 °C. 0.1 mg/mL HC-Ni-LnNPs nanoprobe and various concentrations of GSH were added into the buffer and then incubated for 1 h. Luminescence in the range of 1450 nm to 1600 nm was measured using an 808-nm laser as excited light source.

Selectivity Investigation of HC-Ni-LnNPs. 1 mM GSH or interfering substances were added into the solution of HC-Ni-LnNPs nanoprobe in HEPES (100 mM, pH=7.2). After incubation for 1 h at 37 °C, the luminescence intensity around 1530 nm was measured, excited by 808-nm laser.

Stability Study of HC-Ni-LnNPs and HC-SG-LnNPs. To study the stability, HC-Ni-LnNPs (0.1 mg/mL) was incubated at 37 °C in different medium including 100 mM HEPES (pH=7.2), DMEM medium and FBS, respectively. A part of the mixture was drawn off at different time points to measure the luminescence intensity. The pH stability of HC-Ni-LnNPs was performed in phosphate buffer with different pH. The stability of the product of HC-Ni-LnNPs reacted with GSH, HC-SG-LnNPs, was also conducted in the above three mediums. The luminescence spectra were acquired after incubation for 1 h. All the samples were excited by 808-nm laser.

Cell Culture. 4T1 cells were cultured in 96-well plate or 35 nm glass-bottomed dishes in Dulbecco's modified Eagle's medium (DMEM) supplemented with 100 mg/mL streptomycin, 10% fetal bovine serum and 100 U/mL penicillin at 37 °C in 5% CO_2 atmosphere.

Cytotoxicity. Various concentrations (0-0.6 mg/mL) of HC-Ni-LnNPs were incubated with 4T1 cells for 24 h. The cytotoxicity was then evaluated by CCK-8 assay and Calcein-AM and PI co-staining.

For CCK-8 assay: The cells were incubated for another 4 h after addition of 10 μL CCK-8 reagent in each well, which could be reduced to formazan by dehydrogenase produced by live cells. The water-soluble formazan was quantified through UV-vis spectrophotometry. Cell viability (%) was calculated by (mean Abs. of HC-Ni-LnNPs treated wells/mean Abs. of control wells) × 100%. Each concentration was performed in six replicates.

For calcein-AM and PI co-staining: The cells were co-stained by calcein-AM (2 μM) and PI (4.5 μM) in FBS-free DMEM medium at 37 °C for 30 min. Confocal laser scanning microscope (Zeiss LSM 880 Microscope) was used to record the fluorescence images. Calcein-AM and PI were excited at 488 nm and 561 nm, and the emission in the range of 500-550 nm and 580-650 nm were collected, respectively.

***In Vivo* Toxicity.** Different dosages of HC-Ni-LnNPs (0, 3 and 4.5 mg/100 g body weight) were i.v. injected into health female Balb/c mice with a body weight of about 20 g. The blood and major organs (heart, spleen, liver, lung and kidney) were obtained for hematology analysis and H&E staining, respectively.

***In Vivo* Detection of GSH in NMM-Treated Mice.** Female Balb/c (about 20 g) were i.v. injected with various concentrations of NMM (0, 0.5, 1, 1.5 and 2 mg/100 g body weight) in 100 μL physiological saline for 0.5 h, after that HC-Ni-LnNPs (3 mg/mL, 100 μL) were i.v. injected. Luminescence imaging was conducted 4 h later using NIR II fluorescent imaging system (808-nm excitation, 1300 nm LP filter, power density on the surface of mice was set to 80 mW/cm^2, exposure time was set to 100 ms).

***In Vivo* Monitoring GSH in LPS Induced Inflammation.** 100 μL LPS with various concentrations (0, 0.125, 0.25, 0.75 mg/100 g body weight) in physiological saline were intraperitoneally (i.p.) injected into female Balb/c mice (about 20 g) for 24 h. HC-Ni-LnNPs (3 mg/mL, 100 μL) was intravenously (i.v.) injected and luminescence images were recorded at different time points (808-nm excitation, 1300 nm LP filter, power density on the surface of mice was set to 80 mW/cm^2, exposure time was set to 100 ms).

***In Vivo* Imaging GSH in APAP-Induced Liver Injury.** Female Balb/c mice with body weight of about 20 g were i.v. injected with 100 μL APAP with different concentrations (0, 10, 20, 30 mg/100 g body weight) for 0.5 h. 100 μL HC-Ni-LnNPs (3 mg/mL) was then i.v. injected 4 h before imaging (808-nm excitation, 1300 nm LP filter, power density on the surface of mice was set to 80 mW/cm^2, exposure time was set to 100 ms). In the groups for studying the protective effect of α-LA, the mice were i.v. injected with different dosages of α-LA (1 and 2 mg/100 g body weight) for 1 h before treated with APAP (30 mg/100g body weight).

***In Vivo* Imaging the GSH in Lymphatic Drainage.** Female Balb/c mice with body weight of about 20 g were intradermally (i.d.) injected with different concentrations of LPS dissolved in25 μL physiological saline (0, 0.125, 0.25 and 0.5 mg/100 g body weight). After the injection for 6 h, 25 μL of HC-Ni-LnNPs (10 mg/mL) was i.d. injected. The luminescence images were acquired for 1 h later (808-nm excitation, 1300 nm LP filter, power density on the surface of mice was set to 80 mW/cm^2, exposure time was set to 100 ms).